Section 1

Atmospheric data assimilation schemes, analysis and initialization, data impact studies, observing system experiments

Diurnal Variation of Thermodynamic Environments for Convective Cloud Development around the Central Mountains in Japan during Warm Seasons

Kentaro Araki[1], Masataka Murakami[2], Teruyuki Kato[1], and Takuya Tajiri[1]

1: Meteorological Research Institute, Tsukuba, Ibaraki, Japan

2: Institute for Space-Earth Environmental Research, Nagoya University, Nagoya, Aichi, Japan

e-mail: araki@mri-jma.go.jp

1. Introduction

Convective clouds often develop in the afternoon of summertime fair-weather days around the Central mountains in Japan. Forecasters have traditionally diagnosed the thermodynamic environments for convective cloud development using operational radiosonde data in the morning, at 09 JST (JST=UTC+9h), of the day, because the forecast of these small-scale convective activity by operational mesoscale models still remain a challenge. Vertical structure of the dynamic and thermodynamic environments for the convective cloud development and their diurnal variation have also not been well understood because of temporally sparse observation data. In this study, diurnal variation of thermodynamic environments for both active and non-active convection cases were statistically investigated using the data from a ground-based microwave radiometer (MWR), surface weather observation system, and radiosonde in July and August from 2012 to 2014.

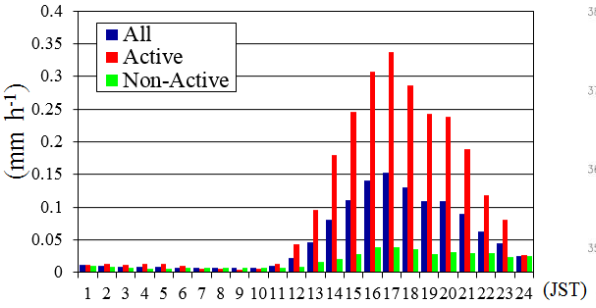

Figure 1. Diurnal variations of hourly RA_{ave} (mm h^{-1}) in (a) the Central Mountain region (137°E–141°E, 34.5°N–38°N) for extracted fair-weather cases. Red, blue, and green bars respectively indicate the average of all (29 samples), active (11 samples), and non-active cases (18 samples).

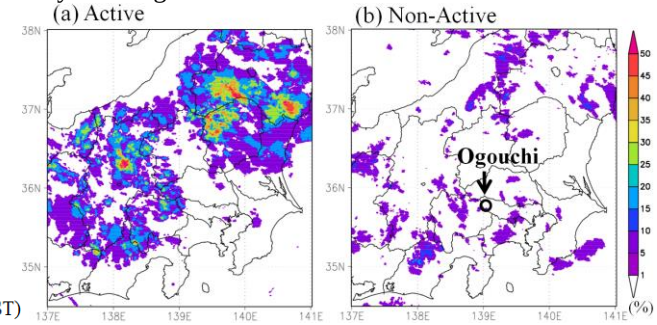

Figure 2. Horizontal distributions of occurrence frequency of rainfall greater than 1 mm h^{-1} at 17 JST for (a) active and (b) non-active cases.

2. Diurnal variation of thermodynamic environments derived from 1DVAR and NHM

Firstly, summertime fair-weather days without precipitation in the morning, which were determined by surface weather map, surface temperature and precipitation observations, were classified into active and non-active convection cases according to the area-averaged rainfall from Radar-AMeDAS Analysis (RA_{ave}). The RA_{ave} was defined as the 1-hour precipitation averaged for the Central Mountain region in Fig. 2. The peak of hourly RA_{ave} was found at 17 JST for all extracted fair-weather cases (Fig. 1). The RA_{ave} of 0.15 mm h^{-1} at 17 JST was used as a criterion between active and non-active convection cases. Active and non-active cases also had peaks of hourly RA_{ave} at 17 JST, and the peak values of RA_{ave} at 17 JST for active and non-active cases were twice greater and smaller than that for all cases, respectively (Fig. 1). Horizontal ditsributions of occurrence frequency of RA larger than 1 mm h^{-1} at 17 JST showed that much precipitation events occurred, especially around high-altitude mountain regions, in active cases (Fig. 2).

Vertical profiles of atmospheric temperature and water vapor were retrieved by a one-dimensional variational (1DVAR; Araki et al. 2014, 2015) technique combining the MWR observation data and the results of the Japan Meteorological Agency Non-Hydrostatic Model (NHM; Saito et al. 2006) simulations. We used the ground-based multi-channel MWR (MP-3000A, Radiometrics) installed at Ogouchi (35.79°N, 139.05°E; Fig. 2) in this study. The MWR observes the brightness temperatures of 35 microwave channels at 22–30 and 51–59 GHz and the radiation temperature of zenith-looking infrared channel (wavelength of 9.6–11.5 μm) at time intervals of a few minutes. A rain sensor is combined with the MWR, and the MWR data up to 10 minutes before rain onset was not used for the retrievals. Numerical experiments were performed using NHM with a horizontal grid spacing of 2 km and a model domain covering the Central Mountain regions, and the 24-hour atmospheric conditions were simulated from 00 JST for all cases. The initial and boundary conditions were taken from 3-hourly JMA mesoscale analyses, and other setups were the same as those used in Saito et al. (2006). The NHM-derived vertical profiles at Ogouchi were interpolated to MWR observation times and used for the 1DVAR retrievals. It was confirmed that 1DVAR-derived profiles were more reliable than NHM-simulated profiles by comparison with radiosonde data, surface weather data, and cloud base temperature obtained from an infrared radiometer. The detail of the validation of the vertical thermodynamic profiles derived from 1DVAR and NHM is given in Araki et al. (2016).

In order to investigate the diurnal variations of thermodynamic environments for both active and non-active cases, diurnal variations of following stability indices were statistically examined; precipitable water vapor (PWV), lifted condensation level (LCL), level of free convection (LFC), convective available potential energy (CAPE), Showalter stability index (SSI), lifted index (LI), K index (KI), and Total Totals index (TTI). The LCL, LFC and CAPE were calculated under the assumption that air parcel averaged over 0–500 m altitudes is lifted. Diurnal variations of these stability indices calculated from 1DVAR- and NHM-derived profiles for active and non-active cases are shown in Fig. 3. Statistical analysis based on the 1DVAR-derived thermodynamic profiles revealed that the LCL increased and the LFC decreased during daytime for both active and non-active cases, whereas the diurnal variation of NHM-derived LCL was unclear in comparison with 1DVAR-derived LCL. The PWV increased during the time period from around 12 to 18 JST for both active and non-active cases, which was suggested that water vapor in the Central Mountain regions increased due to the horizontal advection of low-level water vapor caused by the thermally-induced local circulation (e.g., Sato and Kimura 2005). Stability indices of CAPE, SSI, LI, KI, and LI had similar diurnal variations for both active and non-active cases, although they showed that atmospheric stratification was more unstable for active cases than for non-active cases. Especially for PWV, SSI, LI, KI and TTI, the differences between active and nonactive cases were significant all through the day. In addition, from the results of surface and wind profiler observations, no significant difference between active and non-active cases was found in vertical structure and diurnal variation of thermally-induced local circulations in terms of ability to trigger the convective clouds (not shown).

3. Conclusions and remarks

Diurnal variation of thermodynamic environments for convective cloud development in the Central Mountain regions in Japan in warm seasons was statistically investigated by using the 1DVAR technique combining the MWR data and numerical model simulations. The 1DVAR technique provided realistic and temporally high-resolution thermodynamic profiles in the mountain region, and revealed the detailed diurnal variations of thermodynamic environment for active and non-active convection cases. It was found that the traditional method based on radiosonde observations at 09 JST is of benefit for the diagnosis of the convective activity in the afternoon of the day around the Central Mountains in Japan, even if considering the effect of diurnal variations of the dynamic and thermodynamic environments.

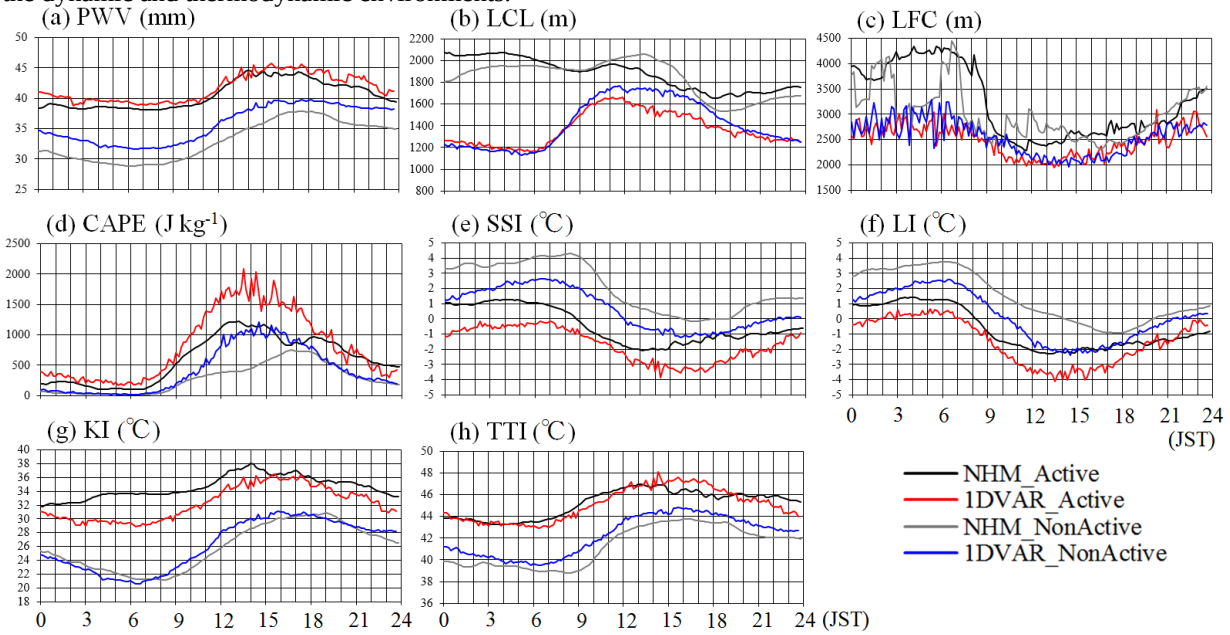

Figure 3. Diurnal variations of stability indices of (a) PWV, (b) LCL, (c) LFC, (d) CAPE, (e) SSI, (f) LI, (g) KI, and (h) TTI calculated by atmospheric thermodynamic profiles derived from NHM-simulation and 1DVAR technique averaged for active and non-active cases.

References:

Araki, K., H. Ishimoto, M. Murakami, and T. Tajiri, 2014: Temporal variation of close-proximity soundings within a tornadic supercell environment. *SOLA*, **10**, 57–61.

Araki, K., M. Murakami, H. Ishimoto, and T. Tajiri, 2015: Ground-based microwave radiometer variational analysis during no-rain and rain conditions. *SOLA*, **11**, 108–112.

Araki, K., and M. Murakami, 2016: Validation of vertical thermodynamic profiles by cloud base temperature obtained from a ground-based infrared radiometer of a mountain region in Central Japan during warm seasons. *CAS/JSC WGNE Research Activities in Atmospheric and Oceanic Modelling*, **46**.

Saito, K., T. Fujita, Y. Yamada, J. Ishida, Y. Kumagai, K. Aranami, S. Ohmori, R. Nagasawa, S. Kumagai, C. Muroi, T. Kato, H. Eito, and Y. Yamazaki, 2006: The operational JMA nonhydrostatic mesoscale model. *Mon. Wea. Rev.*, **134**, 1266–1298.

Sato, T., and F. Kimura, 2005: Diurnal cycle of convective instability around the central mountains in Japan during the warm season. *J. Atmos. Sci.*, **62**, 1626–1636.

The 1-Dimentional Variational Approach to Improve Thermodynamic Profiles in Low-Level Troposphere during Rain Conditions

Kentaro Araki[1], Masataka Murakami[2], Hiroshi Ishimoto[1], and Takuya Tajiri[1]
1: Meteorological Research Institute, Tsukuba, Ibaraki, Japan
2: Institute for Space-Earth Environmental Research, Nagoya University, Nagoya, Aichi, Japan
e-mail: araki@mri-jma.go.jp

1. Introduction

Temporally and spatially high-resolution estimation of thermodynamic environments, especially in the low-level troposphere, is needed for nowcasting and forecasting severe storms. One of the methods for obtaining temporally high-resolution thermodynamic profiles is the retrieval using ground-based microwave radiometer (MWR) data (Araki et al. 2014). The MWR has been used to retrieve vertical profiles of atmospheric temperature and water vapor, and vertically integrated water vapor and liquid water at time intervals of a few minutes. Major methods for the retrieval are neural networks (NNs) and 1-dimensional variational (1DVAR) techniques, and the 1DVAR has been known to outperform other retrieval methods (Araki et al. 2015a). The retrieval using MWR data in zenith direction, however, is critically affected by raindrops on the radome and in the air during rainfall events. In this study, the effectiveness of the off-zenith observations in reducing the error due to raindrops on the radome is investigated (Araki et al. 2015b).

2. Accuracy of retrieved thermodynamic profiles during no-rain and rain conditions

The ground-based multi-channel MWR (model: MP-3000A, Radiometrics) installed on the roof of the Meteorological Research Institute of Japan Meteorological Agency (JMA) at Tateno (36.05°N, 140.13°E) is used in this study. The MWR measures the brightness temperatures of 21 K-band (22–30 GHz) and 14 V-band (51–59 GHz) microwave channels with the band width of 300 MHz in zenith direction and at an elevation angle of 15° in north and south azimuth directions. A rain sensor is also attached to the MWR. In this study, both the 1DVAR technique developed by Araki et al. (2015b) and the NN were used for retrievals using MWR data in zenith and off-zenith directions. The first guess for the 1DVAR was provided from numerical simulations by the JMA non-hydrostatic model (NHM; Saito et al. 2006) with horizontal grid spacing of 5km. The details of the model setting are given in Araki et al. (2015b). In this study, NN-, NHM-, and 1DVAR-derived profiles averaged over 30 min before each radiosonde observation at both 00 and 12 UTC at Tateno were compared with radiosonde-measured profiles of temperature and water vapor density from 25 April to 27 June 2012. To investigate the accuracy of the retrieved profiles under each weather condition, the data were classified into the following three types: No-Rain cases in which rain sensor did not detect rain for 1 h before and after the radiosonde observations (87 samples), Rain_RR<1 cases in which rain sensor detected rain and rain gauge at Tateno observed the 2-hour (1 h before and 1 h after the radiosonde observations)-averaged rainfall rates (RR) less than 1.0 mm h^{-1} (24 samples), and Rain_RR>1 cases in which the 2-hour-averaged RR was equal to or larger than 1.0 mm h^{-1} (10 samples).

Figure 1 shows the vertical profiles of mean difference (MD) and root-mean-square (RMS) error of NN-, 1DVAR-, and NHM-derived atmospheric temperature with respect to radiosonde-measured profiles. The inferiors of Z and OZ in NN and 1DVAR respectively indicate the retrievals using zenith and off-zenith observations in southern azimuth directions. Figure 2 is same as Fig. 1 but for water vapor density. The NHM- and 1DVAR-derived temperature profiles for No-Rain cases showed good agreement: the absolute MD was less than 1 K at all altitudes (Fig. 1a). The RMS errors for 1DVAR-derived temperatures were about 1 K at all altitudes, but those of NHM-derived temperatures reached 1.5 K below 0.5 km (Fig. 1b). The absolute MD for 1DVAR- and NHM-derived water vapor densities for No-Rain cases were less than 0.5 g m^{-3} at all altitudes, and the values of 1DVAR-derived water vapor densities were less than those derived from NHM (Fig. 2a). The RMS errors for 1DVAR-derived vapor density were also less than those derived from NHM at all altitudes; their maximum values for 1DVAR- and NHM-derived vapor densities reached 1.5 and 2 g m^{-3}, respectively, at around 1 km (Fig. 2b). These results show that, compared to other methods, the 1DVAR technique significantly improves the atmospheric temperature profile in the low troposphere and the water vapor profile at all altitudes.

For the cases of Rain_RR<1, NN_Z- and $1DVAR_Z$-derived profiles were affected by rain and the errors in the profiles increased (Figs. 1 and 2). The absolute MD and RMS error for NN_{OZ}-derived temperature and water vapor density were similar to those for the No-Rain case. These results indicate that off-zenith observations reduced the error due to raindrops on the radome for Rain_RR<1 cases. The absolute MD of $1DVAR_{OZ}$-derived temperatures was about 1 K below 1 km and less than 0.5 K above 1.5 km, and the absolute MD of NHM-derived temperatures was 0–0.7 K less than those of $1DVAR_{OZ}$-derived temperature below 1 km. The RMS error was 0.5–1.3 K above 0.5 km, but the error of $1DVAR_{OZ}$-derived temperatures was about 0.5 K smaller than that derived from NHM below 0.5 km. These results suggest that mean biases in 1DVAR-derived temperature profiles, obtained from off-zenith observations, are slightly larger than those of NHM-derived temperature profiles below 1

km under rainy conditions with RR less than 1.0 mm h^{-1}. However, the 1DVAR technique using off-zenith observations could improve the temperature profiles obtained from NHM simulation when NHM simulations show large errors, especially in the lower troposphere. Similar feature was found in water vapor density profiles derived from 1DVAR. For the cases of Rain_RR>1, NN_Z- and $1DVAR_Z$-derived profiles were highly affected by rain (Figs. 1 and 2). Although the accuracies of NHM-derived temperature and vapor density were similar to the cases of Rain_RR<1, the absolute MD and RMS error for $1DVAR_{OZ}$-derived profile of both temperature and vapor density were larger below 1–2 km. The RMS error for NN_{OZ}-derived profiles was larger than that of $1DVAR_{OZ}$-derived profile for temperature at all altitudes and for vapor density above 0.5 km, respectively. These results indicate that the 1DVAR technique outperforms the NN technique in retrievals of thermodynamic profiles under conditions of heavy rain, whereas the 1DVAR technique does not improve the accuracy of thermodynamic profiles when compared with NHM simulation results.

3. Conclusions and remarks

The 1DVAR technique that uses MWR data was applied for no-rain and rainy conditions and the effect of off-zenith observations on reducing the error during rain periods was statistically investigated. Comparisons with radiosonde observations show that the 1DVAR technique used in this study successfully improves the vertical profiles of temperature in the low troposphere and those of water vapor density at all altitudes, as compared to retrievals by neural networks and the results of numerical simulation under no-rain conditions. There is also indication that the error in the retrieved profiles could be reduced by the 1DVAR technique by using off-zenith observations at an elevation angle of 15° even under rain conditions with rainfall rates less than 1.0 mm h^{-1}, especially when the numerical model does not accurately reproduce the thermodynamic environment. This result suggests that the 1DVAR technique is helpful in nowcasting severe storms.

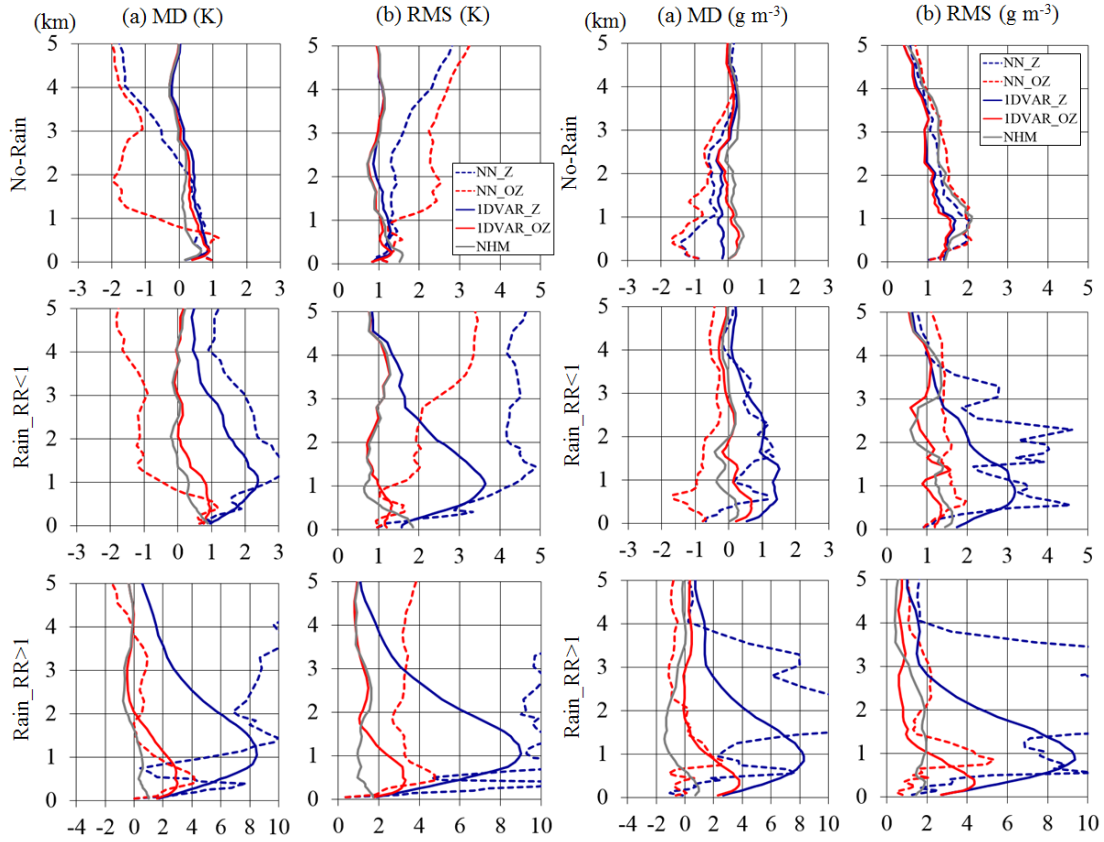

Figure 1. (a) Mean difference (MD) and (b) root-mean-square (RMS) error of NN-, 1DVAR-, and NHM-derived atmospheric temperature with respect to radiosonde soundings.

Figure 2. Same as Fig. 1, but for water vapor density.

References:

Araki, K., H. Ishimoto, M. Murakami, and T. Tajiri, 2014: Temporal variation of close-proximity soundings within a tornadic supercell environment. *SOLA*, **10**, 57–61.

Araki, K., M. Murakami, H. Ishimoto, and T. Tajiri, 2015a: The impact of ground-based microwave radiometer data to estimation of thermodynamic profiles in low-level troposphere. *CAS/JSC WGNE Research Activities in Atmospheric and Oceanic Modelling*, **45**, 1.03–1.04.

Araki, K., M. Murakami, H. Ishimoto, and T. Tajiri, 2015b: Ground-based microwave radiometer variational analysis during no-rain and rain conditions. *SOLA*, **11**, 108–112.

Saito, K., T. Fujita, Y. Yamada, J. Ishida, Y. Kumagai, K. Aranami, S. Ohmori, R. Nagasawa, S. Kumagai, C. Muroi, T. Kato, H. Eito, and Y. Yamazaki, 2006: The operational JMA nonhydrostatic mesoscale model. *Mon. Wea. Rev.*, **134**, 1266–1298.

Validation of Vertical Thermodynamic Profiles by Cloud Base Temperature Obtained from a Ground-Based Infrared Radiometer in a Mountain Region of Central Japan during Warm Seasons

Kentaro Araki[1] and Masataka Murakami[2]

1: Meteorological Research Institute, Tsukuba, Ibaraki, Japan

2: Institute for Space-Earth Environmental Research, Nagoya University, Nagoya, Aichi, Japan

e-mail: araki@mri-jma.go.jp

1. Introduction

Accurate estimation of thermodynamic profiles is required for nowcasting severe storms and diagnosing their environmental conditions. Forecasters have traditionally diagnosed convective cloud development in the Central Mountain regions in Japan in warm seasons by using 12-hourly operational radiosonde observations at Tateno (36.05°N, 140.13°E) in the plain region. However, vertical structure of thermodynamic environments for such convective cloud development and their diurnal variations have not been well understood. In general, mesoscale numerical weather models often fail to reproduce diurnal variations of atmospheric conditions in the boundary layer (e.g., Hanna and Yang 2001). Some studies also reported that the errors of forecasts for atmospheric fields in the boundary layer increase in complex terrains (e.g., Zhang et al. 2013).

Recently, the one dimensional variational (1DVAR; Araki et al. 2015) technique combining a ground-based microwave radiometer (MWR) data with results of numerical model simulations has been known to outperform other methods in estimating thermodynamic profiles in the low-level troposphere. Araki et al. (2016) statistically investigated the diurnal variation of the thermodynamic environment for convective cloud development in the Central Mountain regions using 1DVAR-retrieved vertical thermodynamic profiles based on the MWR observations at Ogouchi (35.79°N, 139.05°E) in the mountain region. They reported that the lifted condensation level (LCL) derived from 1DVAR-retrieved profiles increased during daytime, although the diurnal variation of LCL derived from the Japan Meteorological Agency Non-Hydrostatic Model (NHM; Saito et al. 2006) was unclear. The purpose of this study is to validate the NHM-simulated and 1DVAR-retrieved thermodynamic profiles using cloud base temperature obtained from ground-based infrared radiometer data.

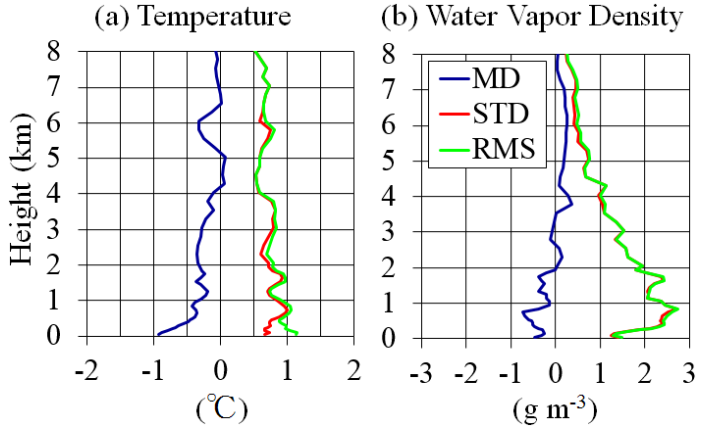

Figure 1. Comparisons between NHM-simulated and observed vertical profiles for (a) temperature (°C) and (b) water vapor density (g m^{-3}) at Tateno. Blue, red, and green lines respectively indicate the MD, STD, and RMS difference of NHM-simulated profiles with respect to observations.

Table 1. MDs, STDs, and RMS differences of NHM-simulated (a) surface temperature (°C) and (b) water vapor mixing ratio (g kg^{-1}) with respect to surface observations at Tateno and Ogouchi at 09 and 12 JST.

(a) Temperature (°C)

	MD	STD	RMS
Tateno 09	-1.20	0.93	1.52
Tateno 12	-0.66	0.88	1.10
Ogouchi 09	-0.14	1.50	1.21
Ogouchi 12	-2.07	1.11	2.18

(b) Mixing ratio of water vapor (g kg^{-1})

	MD	STD	RMS
Tateno 09	-0.2	1.23	1.25
Tateno 12	-2.33	1.59	2.83
Ogouchi 09	-3.21	1.26	3.45
Ogouchi 12	-2.65	1.29	2.94

2. Verification of the NHM-simulated and 1DVAR-retrieved thermodynamic profiles

In this study, the 1DVAR technique developed by Araki et al. (2015) was applied to retrieve atmospheric temperature and water vapor profiles at Ogouchi, where the NHM-simulated temperature and humidity profiles (first guesses) are adjusted by assimilating the MWR (MP-3000A, Radiometrics) data of the brightness temperatures (TBs) at 22–30 and 51–59 GHz. The details of the 1DVAR and model settings are given in Araki et al. (2016). The infrared radiometer is attached to the MWR and observes the infrared TB (wavelength of 9.6–11.5 μm) in zenith-looking mode, which provides cloud base information. Vertical thermodynamic profiles derived from 1DVAR and NHM were validated for 29 summertime fair-weather days from 2011 to 2013 selected by Araki et al. (2016).

In order to evaluate the accuracy of NHM-simulated vertical profiles of atmospheric temperature and water vapor, results of the simulations were compared with operational radiosonde observations at Tateno at 09 JST (JST=UTC+9h) for all cases (Fig. 1). Absolute mean differences (MDs) of NHM-simulated temperature and water vapor density with respect to radiosonde observations were respectively 0.5–1.0 °C and 0.2–1.0 g m^{-3} at altitudes less than 2 km, and absolute MDs, standard deviations (STDs), and root-mean-square (RMS) differences were

large in low-level troposphere for both temperature and water vapor density. On the other hand, errors of temperature and water vapor density were relatively small at altitudes above 2 km. Table 1 shows the MDs, STDs, and RMS differences of NHM-simulated surface temperature and water vapor mixing ratio with respect to surface observations at Tateno and Ogouchi at 09 and 12 JST. The absolute MDs, STDs, RMS differences of NHM-simulated surface temperature were 0.6–1.0 °C at both 09 and 12 JST (Table 1a). Although these values for Ogouchi at 09 JST were similar to those for Tateno, the absolute MD and RMS difference of surface temperature reached 2 °C at 12 JST. With respect to waetr vapor mixing ratio, the absolute MD and RMS difference became larger at Tateno from 09 to 12 JST. At Ogouchi, the absolute MD and RMS difference at both 09 and 12 JST were similar to those at Tateno at 12 JST. These results suggested that the NHM-simulated thermodynamic environments had significant errors near the surface and in low-level troposphere, and that the errors in the plain region increased during daytime but the errors in the mountain region were large all through the day. Since the 1DVAR technique especially improves low-level thermodynamic profiles (Araki et al. 2015), it's promising that the 1DVAR-retrieved thermodynamic profiles at Ogouchi would be reliable.

To verify the 1DVAR- and NHM-derived thermodynamic profiles, precipitable water vapors (PWVs) obtained from each water vapor profile were firstly compared with PWVs retrieved from MWR neural network (NN) technique (Fig. 2), which was confirmed to be accurate as same as GPS-derived PWV (Araki et al. 2014). The MD and RMS difference of 1DVAR-derived PWVs were respectively –1.1 and 1.8 mm, although those of NHM-derived PWVs were –3.1 and 4.0 mm. Secondly, cloud base temperature (same as TB) observed by infrared radiometer and temperature at the LCL derived from 1DVAR and NHM were compared (Fig. 3). In this comparison, assuming shallow cumulus formation before the convective cloud development in the afternoon, 10-minute maximum TBs higher than 10 °C, which were measured with the infrared radiometer from 09 to 12 JST, were used in the comparison. The MD and RMS difference of 1DVAR-derived LCL temperature were 0.0 and 1.6 K, although those of NHM-derived LCL temperature were –2.4 and 3.2 K. The difference of NHM-derived LCL temperature increased during the time period from 11 to 12 JST. These results show that the 1DVAR technique successfully outperformed the NHM simulation in estimating vertical thermodynamic profiles.

3. Conclusions and remarks

Vertical thermodynamic profiles derived from 1DVAR and NHM simulations at Ogouchi during warm seasons were verified by using MWR and infrared radiometer data. It's confirmed that the 1DVAR technique successfully provided reliable temperature and water vapor profiles, and that vertical structures of thermodynamic profiles and their diurnal variations can be discussed by using 1DVAR-derived profiles in Araki et al. (2016). For numerical model developments, it's desired that the physical processes of the boundary layer, radiation, and land-surface condition would be improved.

References:

Araki, K., H. Ishimoto, M. Murakami, and T. Tajiri, 2014: Temporal variation of close-proximity soundings within a tornadic supercell environment. *SOLA*, **10**, 57–61.

Araki, K., M. Murakami, H. Ishimoto, and T. Tajiri, 2015: Ground-based microwave radiometer variational analysis during no-rain and rain conditions. *SOLA*, **11**, 108–112.

Araki, K., M. Murakami, T. Kato, and T. Tajiri, 2016: Diurnal variation of thermodynamic environments for convective cloud development around the Central Mountains in Japan during warm seasons. *CAS/JSC WGNE Research Activities in Atmospheric and Oceanic Modelling*, **46**.

Saito, K., T. Fujita, Y. Yamada, J. Ishida, Y. Kumagai, K. Aranami, S. Ohmori, R. Nagasawa, S. Kumagai, C. Muroi, T. Kato, H. Eito, and Y. Yamazaki, 2006: The operational JMA nonhydrostatic mesoscale model. *Mon. Wea. Rev.*, **134**, 1266–1298.

Hanna, S. R., and R. Yang, 2001: Evaluations of mesoscale models' simulations of near-surface winds, temperature gradients, and mixing depths. *J. Appl. Meteor.*, **40**, 1095–1104.

Zhang, H., Z. Pu, and X. Zhang, 2013: Examination of errors in near-surface temperature and wind from WRF numerical simulations in regions of complex terrain. *Wea. Forecasting*, **28**, 893–914.

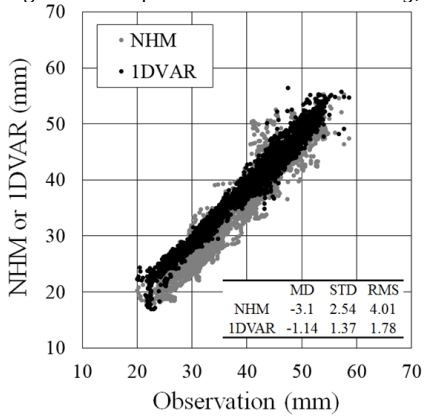

Figure 2. Comparisons of NHM- (gray) and 1DVAR-derived PWVs (black) with NN-derived PWVs.

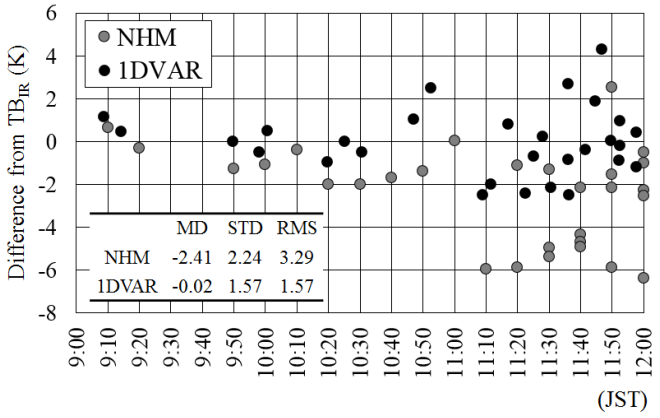

Figure 3. Time series of the differences of atmospheric temperature (K) at the level of LCL in NHM- (gray) and 1DVAR-derived thermodynamic profiles (black) from the brightness temperature (TB; K) obtained from infrared channel.

Improvement of JMA's Meso-scale Analysis background errors

Junya Fukuda, Toru Tsukamoto, Tadashi Fujita
Numerical Prediction Division, Japan Meteorological Agency
1-3-4 Otemachi, Chiyoda-ku, Tokyo 100-8122, Japan
E-mail: jfukuda@met.kishou.go.jp, t_tsukamoto@met.kishou.go.jp, t-fujita@met.kishou.go.jp

1. Introduction

JMA's Meso-scale NWP system incorporates forecast called Meso-Scale Model (MSM) and objective analysis called Meso-scale Analysis (MA) using 4D-Var data assimilation. Recent investigation showed that the background error (BGE) covariance of the MA, which had been unchanged since 2009, was no longer consistent with the error characteristics of the first guess in the current system. Single observation experiments also revealed that related modeling often resulted in artificial analysis increments. To address these problems, the forecast error statistical samples needed for evaluation of BGE covariance were updated and the modeling approach was revised. The details and impacts of these changes are described below.

2. Details of changes

i) Update of forecast error statistical samples

The BGE covariance of MA is evaluated using the NMC method (Parrish and Derber 1992) with statistical processing of forecast error samples over a long period. The previous BGE covariance was evaluated from operational MSM runs covering data for 2005. In order to more appropriately represent error characteristics in the current Meso-scale NWP system, the error statistics were updated using samples obtained from the latest 2014 – 2015 MSM runs. The new BGE variances were approximately halved, while the vertical correlation was left largely unchanged and the horizontal correlation became only slightly shorter.

ii) Revision of BGE covariance modeling

The modeling of BGE covariance is based on eigenvalue decomposition of vertical error covariance. The previous modeling involved specification of the horizontal error correlation in the eigen space, and correlations among different eigen modes were ignored. As a result, horizontal correlations in the real space transformed from the eigen space were non-trivial and deviated from actual values, causing artificial analysis increments. To address this, the modeling of BGE covariance was revised so that the horizontal correlation is specified in real space (Bannister 2003), making it closer to the actual values.

3. Single observation experiments

The new BGE was developed using updated forecast error samples and by applying the new modeling as discussed in Section 2. Assimilation tests based on single observations with 3D-Var revealed the specific properties of the updated and previous BGEs. Figure 1 shows a typical difference in increments from the two assimilations using the same background and observation. Figure 1 (a) with the new BGE shows a weaker increment than (b) with the old BGE, corresponding to smaller variance of the updated BGE. In addition, the previous BGE modeled in the eigen space did not provide a true representation of the actual error profile in the real space, and produced widely spreading increments. In extreme cases, the previous BGE generated completely distorted increments as shown in Fig. 2.

4. Impact of the updated BGE on MA and MSM

A one-month analysis-forecast cycle experiment indicated that the new BGE had positive impacts on the operational MA and MSM. In this real-case experiment, increments were generally small due to the minor variance of the updated BGE, and analysis values showed farther departure from observations in the assimilation window (three hours up to the initial forecast time) than in the experiment with the previous BGE. The departure from observation values

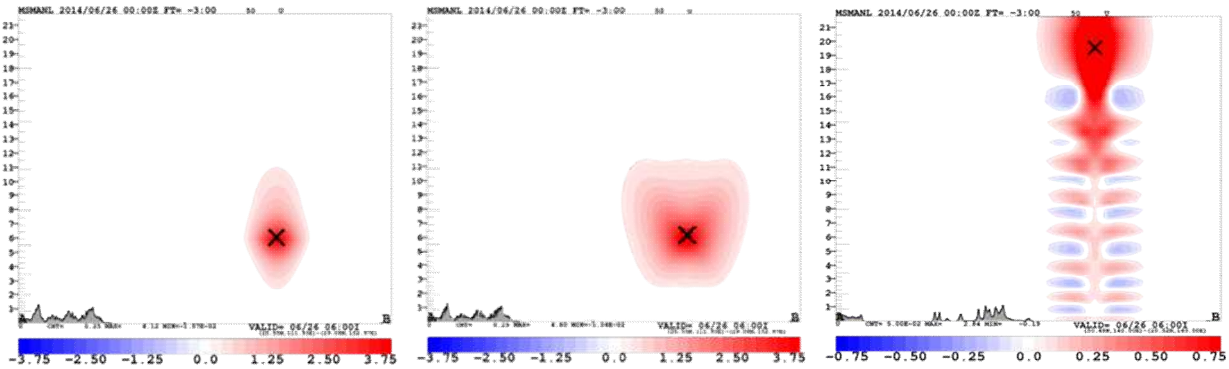

Fig. 1. Analysis increments from a 3D-Var run with (a) the updated BGE and (b) the previous BGE based on assimilation of a single zonal wind observation (marked ×) with a value 5 m/s above the background value (observation error: 1 m/s). The figure shows a north-south vertical cross section.

Fig. 2. Analysis increment from a 3D-Var run with the previous BGE based on assimilation of a single zonal wind observation (marked ×) with a value 5 m/s above the background value (observation error: 1 m/s). The figure shows an east-west vertical cross section.

decreased in the next three-hour forecast for most types of assimilated observations. In addition, sound and gravity wave oscillation and rapid drift of temperature, water vapor and wind in the early stages of forecasts are moderated. It can be inferred that analysis with the previous BGE resulted in excessive reliance on observations.

A supplementary experiment indicated that both the forecast sample updates and the covariance modeling revision helped to improve precipitation prediction accuracy. By way of example, in the experiment with the updated BGE, heavy rain in the Tohoku region was consistently predicted with locational accuracy despite long lead times of up to 39 hours (Fig. 3; 36-hour forecast). Warm moisture flowing from Typhoon Neoguri (located west of the region in the figure) toward the Baiu front also appears to be represented more adequately.

5. Summary

JMA has improved its MA BGE covariance with updated forecast error statistical samples and a revision of related modeling. The issue of artificial analysis increments was solved by the change in covariance modeling. The smaller variances from the updated BGE enhance the balance of the analysis, leading to moderation of undesirable oscillation and drift. The updates have been shown to have improved the accuracy of the Meso-scale NWP system. While analytical balance is affected by both BGE and observation errors, only BGE was updated in this work. Accordingly, optimization of observation errors based on the system with the improved BGE will be addressed as a future task.

References

Bannister, R., 2003: On control variable transforms in the Met Office 3d and 4d Var., and a description of the proposed waveband summation transformation. DARC Internal Report, 5, 45 pp

Parrish, D. and J. Derber, 1992: The National Meteorological Center's Spectral Statistical-Interpolation Analysis System. Mon. Wea. Rev., 120, 1747 – 1763

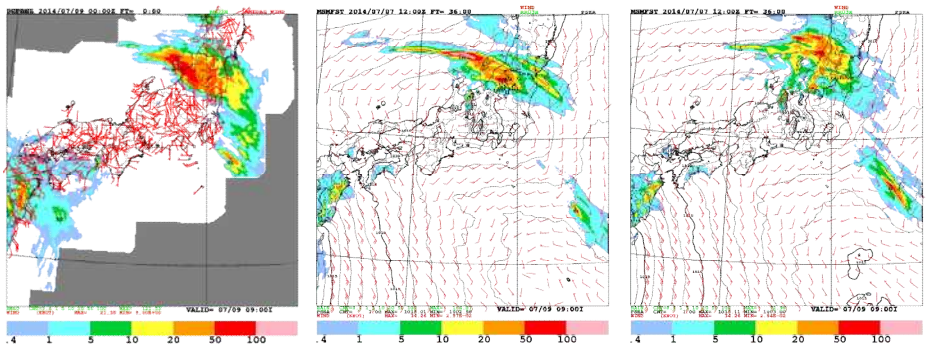

Fig. 3. 3-h accumulated precipitation valid at 00 UTC 9 Jul. 2014. (a) Observation. (b) 6-h forecast with the updated BGE. (c) 6-h forecast with the previous BGE.

Data assimilation using GPM/DPR at JMA

Yasutaka Ikuta

Numerical Prediction Division, Japan Meteorological Agency
E-mail: ikuta@met.kishou.go.jp

1. Introduction

The global precipitation measurement (GPM) core satellite carries a dual-frequency precipitation radar (DPR) incorporating Ku-band precipitation radar (KuPR) and Ka-band precipitation radar (KaPR). The DPR instrument was developed by the Japan Aerospace Exploration Agency (JAXA) in cooperation with the National Institute of Information and Communications Technology (NICT), and observes vertical profiles of reflectivity in the mid-latitude region between 65°S and 65°N. As radar reflectivity profiles are commonly observed on land but rarely at sea, hydrometeor information included in these reflectivity data is very valuable for forecast verification and data assimilation relating to mesoscale phenomena. In evaluation of the impacts of DRP data assimilation to create the initial conditions of JMA's mesoscale model (MSM) with a 5-km horizontal resolution, precipitation forecast improvement was observed despite the narrow swath width of KuPR and KaPR (250 and 150 km, respectively) in comparison to those of other orbit satellite observations. The Japan Meteorological Agency (JMA) began using DPR data in its operational mesoscale NWP system in March 2015. This document outlines the method of DPR assimilation and related impacts.

2. Method

In DPR assimilation, relative humidity (RH) data retrieved from the DPR reflectivity profile using Bayesian theory are assimilated on the basis of 4DVAR (Ikuta, 2014). This method, known as 1D+4DVAR, is also used for assimilation of ground-based weather radar (Ikuta and Honda, 2011). For this assimilation, a new space-borne radar simulator was developed and the previous RH retrieval method used was upgraded.

First, KuPR reflectivity (Z_{Ku}) and KaPR reflectivity (Z_{Ka}) were simulated from MSM outputs using the new space-borne radar simulator. As all hydrometeors are assumed to be spherical in the MSM, the radar cross section is calculated using the Lorenz-Mie theory. To reduce the computation time of the simulator, a Mie-scattering table was formulated in advance.

Second, RH data to be assimilated are retrieved from Z_{Ku} and Z_{Ka} values based on the Bayesian theorem using the predetermined relationship between simulated values of Z_{Ku} and Z_{Ka} and RH for the first guess. As simulated reflectivity from MSM outputs is known to have biases (Eito and Aonashi, 2009), adaptive bias correction is assimilated into the retrieval method via the removal of expected values of observed reflectivity minus simulated reflectivity as a bias from observed reflectivity in the equation used for the prior probability density function. Despite the assimilation of such bias-corrected data, assimilation of ice phase data cancels the water-vapor bias in the upper atmosphere caused by the model's characteristics but reduces the weak precipitation frequency toward the negative bias. Accordingly, only the liquid phase of DPR is currently used in data assimilation.

3. Performance evaluation

An experiment to determine the effects of DPR assimilation was performed in a framework similar to that of the operational mesoscale NWP system. Here, the regular analysis-forecast cycle experiment is referred to as CNTL, and that with DPR assimilation is referred to as TEST. An example of the impact of DPR was observed for a heavy rainfall event (over 160 mm/3 h) during the period from 8 – 10 September 2015. DPR was assimilated at the initial times of 15 UTC on 7 September and 00 UTC on 8 September (Fig. 1) before this severe weather event. In the mesoscale NWP system, the analysis and forecast cycle gains efficiencies from DPR assimilation with each initial condition. As a result, the precipitation forecast with a lead time of 33 hours (Fig. 2) was improved in the TEST run. In addition, even though fewer DPR data are assimilated and the coverage area of DPR is smaller than those of other satellites, statistical evaluation showed improvement at over 10 mm/3 h (Fig. 3). The statistical period examined was from 2 August 2015 to 10 September 2015. The impact in winter was low because ice-phase data were not used. Utilization of such data is key to improving snowfall forecasts in winter.

References

Eito, H. and K. Aonashi, 2009: Verification of Hydrometeor Properties Simulated by a Cloud Resolving Model Using a Passive Microwave Satellite and Ground-Based Radar Observations for a Rainfall System Associated with the Baiu Front. *J. Meteor. Soc. Japan*, **87A**, 425–446.

Ikuta, Y., 2014: Development of GPM/DPR Data Assimilation at JMA. *7th Workshop of the International Precipitation Working Group, 17-21 No-vember 2014*.

Ikuta, Y. and Y. Honda, 2011: Development of 1D+4DVAR data assimilation of radar reflectivity in JNoVA. *CAS/JSC WGNE Res. Activ. Atmos. Oceanic Modell.*, **41**, 01.09–01.10.

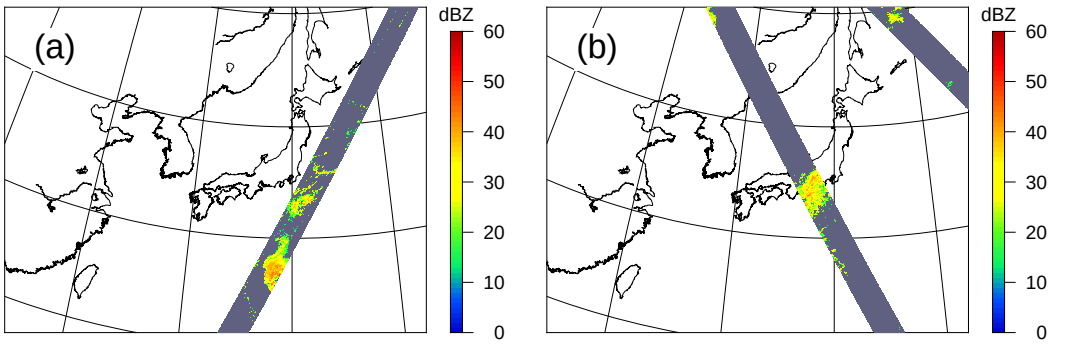

Figure 1. KuPR observation at an altitude of 3,000 m in an assimilation window with the initial times of (a) 15 UTC on 7 September and (b) 00 UTC on 8 September 2015.

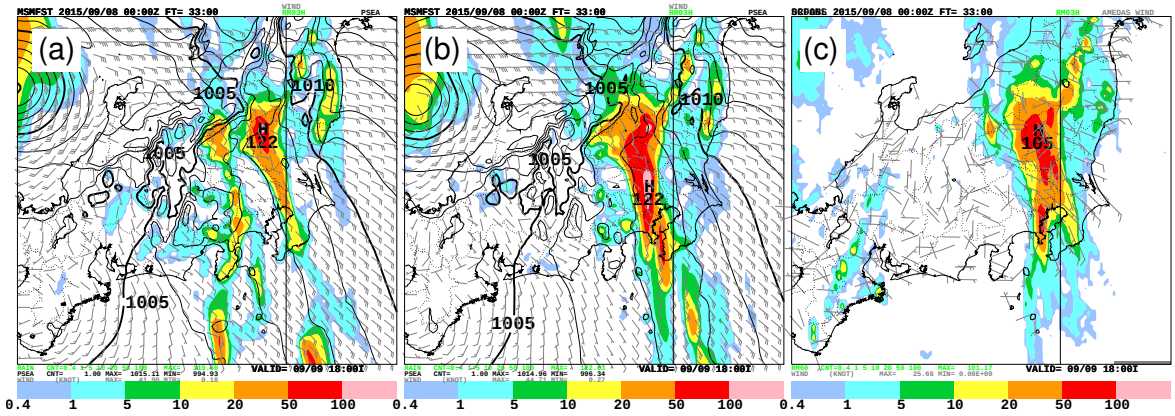

Figure 2. Cumulative three-hour precipitation, surface wind and surface pressure forecasts of (a) CNTL and (b) TEST with a lead time of 33 hours and an initial time of 00 UTC on 8 September 2015, and (c) radar analysis and AMeDAS wind at 03 UTC on 9 September 2015.

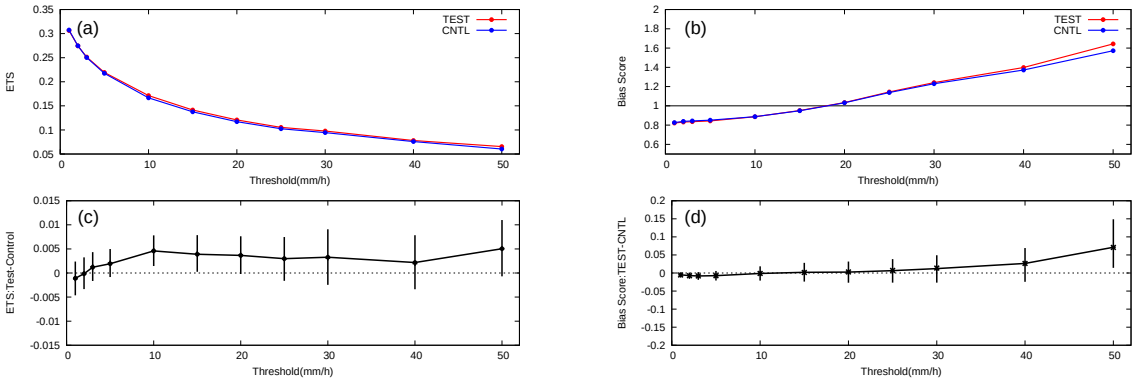

Figure 3. (a) Equitable threat scores (ETS) and (b) bias scores for cumulative three-hour precipitation against radar analysis from 2 August to 10 September 2015. (c) TEST-CNTL of ETS and (d) that of bias score. The error bar represents the 95 % confidence interval.

Assimilation of GPM microwave imager data in JMA's NWP systems

Masahiro Kazumori
Numerical Prediction Division, Forecast Department, Japan Meteorological Agency
Corresponding author: M. Kazumori, JMA, Otemachi, Chiyoda-ku, Tokyo, 100-8122, Japan
E-mail: kazumori@met.kishou.go.jp

Introduction

Accurate forecasts of severe precipitation are essential for mitigating the effects of natural disasters. In this context, space-based microwave imager observations of atmospheric water vapor, cloud and precipitation provide crucial information for real-time environmental monitoring and weather forecasting. The Japan Meteorological Agency (JMA) operates two numerical weather prediction (NWP) models (one global and one regional (mesoscale)) for such forecasting. Both are initialized using four dimensional variational data assimilation systems in which microwave imager observations play important roles in producing accurate initial fields of moisture. In 2015, clear-sky microwave imager radiances from GCOM-W/AMSR2, DMSP-F16, F17 and F18/SSMIS were assimilated into the global and mesoscale NWP systems, and precipitation data retrieved from these radiances were assimilated into the mesoscale NWP system. A new GPM microwave imager (GMI) was launched by NASA and JAXA in February 2014, and related real-time data have been available since March 2014. GMI is the successor to the previous TRMM microwave imager, and continuity of data usage in operational NWP systems must be ensured. Assimilation of data from the new microwave imager is expected to contribute to accurate humidity analysis and precipitation forecasting. The two new GMI water vapor sounding channels at 183+3 and 183+7 GHz are expected to bring further improvement to water vapor analysis in the middle and upper troposphere.

Methodology

Clear-sky radiance data from GMI's 19, 23, 37 and 89 GHz vertical polarized channels and the new 183+3, 183+7 GHz channels are assimilated in the global and mesoscale NWP system. Former low-frequency channels are assimilated as with other microwave imagers [1]. Removal of cloud-affected radiance for 183 GHz channels is based on the GMI window channel's (166 GHz) first-guess departure (observed radiance minus simulated radiance). GMI retrieved precipitation data for assimilation into the mesoscale NWP system are retrieved from the set low-frequency channels using a statistical method [2]. The data coverage of the GMI radiance data and retrieved precipitation data used in JMA's NWP systems is shown in Figure 1.

Assimilation experiments

Assimilation experiments involving GMI radiance data with the global NWP system were conducted for the periods of January 2014 and July 2015, and corresponding experiments were performed with the mesoscale NWP system. The results indicated similar impacts in analysis of water vapor fields between the two systems, which both exhibited better agreement with existing observations. As shown in Figure 2, normalized changes in the standard deviation of the first-guess departure indicate consistent improvement in the water vapor field. Better lower-tropospheric temperature fields were also confirmed from AMSU-A channels 4 and 5. Improvements in MHS channels 3, 4, and 5 were brought by the new 183 GHz GMI channels, as evidenced by the fact that the observation frequency is common to the 183 GHz water vapor absorption band. In the experiments with the mesoscale NWP system, precipitation forecast improvement was confirmed (e.g., Figure 3). Improved water vapor field in the initial condition is considered to have brought realistic precipitation forecasts in the mesoscale NWP system.

Summary

Assimilation of GMI radiance data under clear-sky conditions and retrieved precipitation assimilation showed consistent improvement in water vapor analysis and helped to ameliorate

precipitation forecasts in JMA's NWP systems. The addition of the 183 GHz GMI observation channels brought clear benefits in mid- and upper-tropospheric water vapor analysis. Based on these findings, GMI radiance data are scheduled for assimilation into JMA's operational NWP system in March 2016.

References

[1] Kazumori, M. 2014: Satellite Radiance Assimilation in the JMA Operational Mesoscale 4DVar System. *Mon. Wea. Rev.*, 142, 1361 – 1381. doi: http://dx.doi.org/10.1175/MWR-D-13-00135.1

[2] Takeuchi, Y. and T. Kurino 1997: Document of algorithm to derive rain rate and precipitation with SSM/I and AMSR: Algorithm description of PIs for SSM/I and ADEOS-II/AMSR. Second AMSR Workshop 61.1-61.9, NASDA, Tokyo, Japan

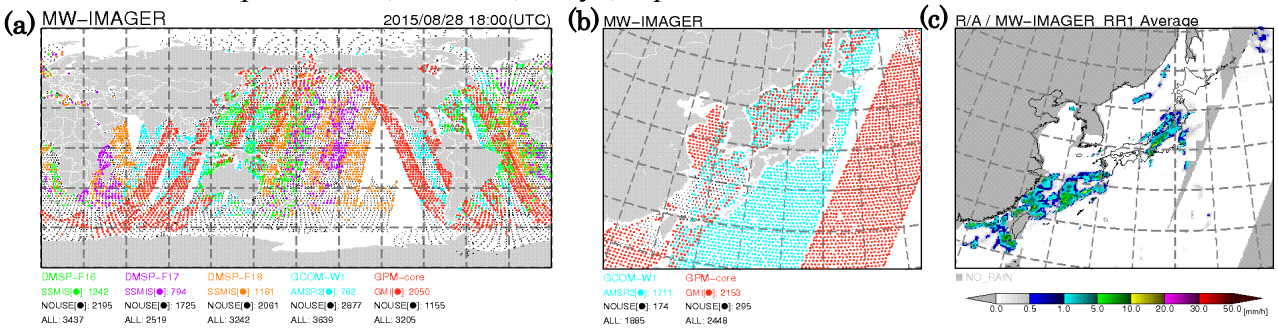

Figure 1. Microwave imager data used in JMA's NWP systems at 18 UTC on August 28 2015. Red dots denote GMI radiance data. (a) Data coverage in the global NWP system. (b) Data coverage in the mesoscale NWP system. (c) Data coverage of precipitation retrieved from microwave imager and ground-based radar in the mesoscale NWP system.

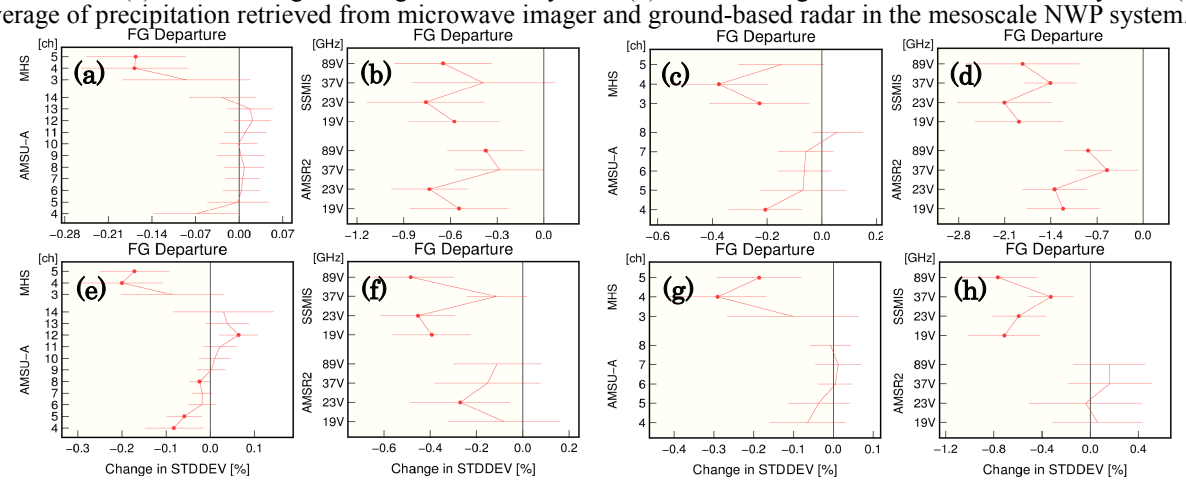

Figure 2. Normalized changes in the standard deviation of first-guess departures from (a) microwave sounding data (b) microwave imager data with assimilation of GMI radiance data in the global NWP system for boreal summer. (c) and (d): as per (a) and (b), but for the mesoscale NWP system. (e), (f), (g) and (h): as per (a) and (b), but for boreal winter. Negative values indicate first-guess field improvement.

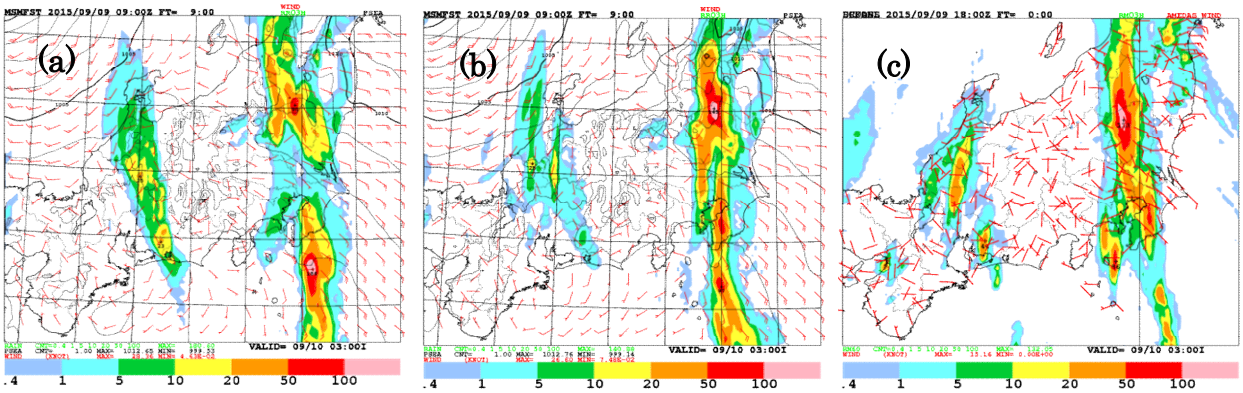

Figure 3. Comparison of three-hour cumulative rainfall forecasts for 00 UTC on September 9 2015. The forecast period is nine hours. (a): CNTL run (without GMI); (b) TEST run (with GMI); (c) rainfall distribution estimated from radar observation and rain gauge data (unit: mm/3 hr).

Assimilation of Himawari-8 clear sky radiance data in JMA's NWP systems

Masahiro Kazumori
Numerical Prediction Division, Forecast Department, Japan Meteorological Agency
Corresponding author: M. Kazumori, JMA, Otemachi, Chiyoda-ku, Tokyo, 100-8122, Japan
E-mail: kazumori@met.kishou.go.jp

Introduction

Clear sky radiance (CSR) data from JMA's new-generation Himawari-8 geostationary meteorological satellite, which was launched on 7 October 2014, have been disseminated operationally to the NWP community since 7 July 2015. These data contain observational information on upper tropospheric water vapor in clear sky conditions, and are provided in temporally and spatially dense form for assimilation in operational NWP systems. Data from three water vapor absorption bands (6.2, 6.9 and 7.3 micrometers, referred to as bands 8, 9 and 10, respectively) are provided. The current horizontal resolution of Himawari-8 CSR data for assimilation is 32 km, and full-disk data are provided every hour.

Data assimilation systems and CSR data processing

JMA operates global DA (data assimilation) and mesoscale DA systems in which CSR data are used. CSR data from the previous MTSAT-2 satellite are assimilated in both. To evaluate Himawari-8 CSR data before their operational use, related first-guess (FG) departure statistics (observed radiance minus calculated radiance) were examined. Improved cloud detection in CSR data production at JMA's Meteorological Satellite Center increases the number of available CSR data, especially over land. Further cloud detection in the preprocessor of the DA systems is based on the clear-pixel ratio of Himawari-8 band 13 (10.4 micrometers). Overall, Himawari-8 CSR data quality is superior to that of MTSAT-2.

Assimilation experiments

Himawari-8 CSR data assimilation experiments were conducted using the global and mesoscale DA systems. In the former, Himawari-8 band 8, 9 and 10 CSR data were assimilated. However, only oceanic data from bands 9 and 10 were assimilated to avoid land surface signal contamination under dry atmospheric conditions. In the mesoscale DA system, band 8 CSR data were assimilated. The data thinning distance was set as 220 km for the global system and 45 km for the mesoscale system. Hourly CSR data were assimilated in both systems.

The assimilation of CSR data in JMA's global DA system reduced dry biases in analyzed water vapor fields in the troposphere and brought better FG fitting to other water vapor-sensitive observations (Figure 1). Assimilation in the mesoscale DA system enhanced water vapor contrast in the troposphere (Figure 2) and contributed to improved presentation of forecast precipitation distribution (Figure 3).

Summary

Himawari-8 CSR data provide much more information on atmospheric water vapor in the troposphere than the previous MTSAT-2 satellite for JMA's DA systems. The data are spatially dense, and observations from multiple water vapor bands are available with an improved cloud screening method. These enhancements contribute to improved water vapor analysis in the DA systems. The area of improvement corresponds to that covered by Himawari-8 observation range. Improvement of water vapor analysis is crucial for the accurate prediction of severe weather phenomena such as the development of tropical cyclones and heavy precipitation caused by stationary fronts in East Asia.

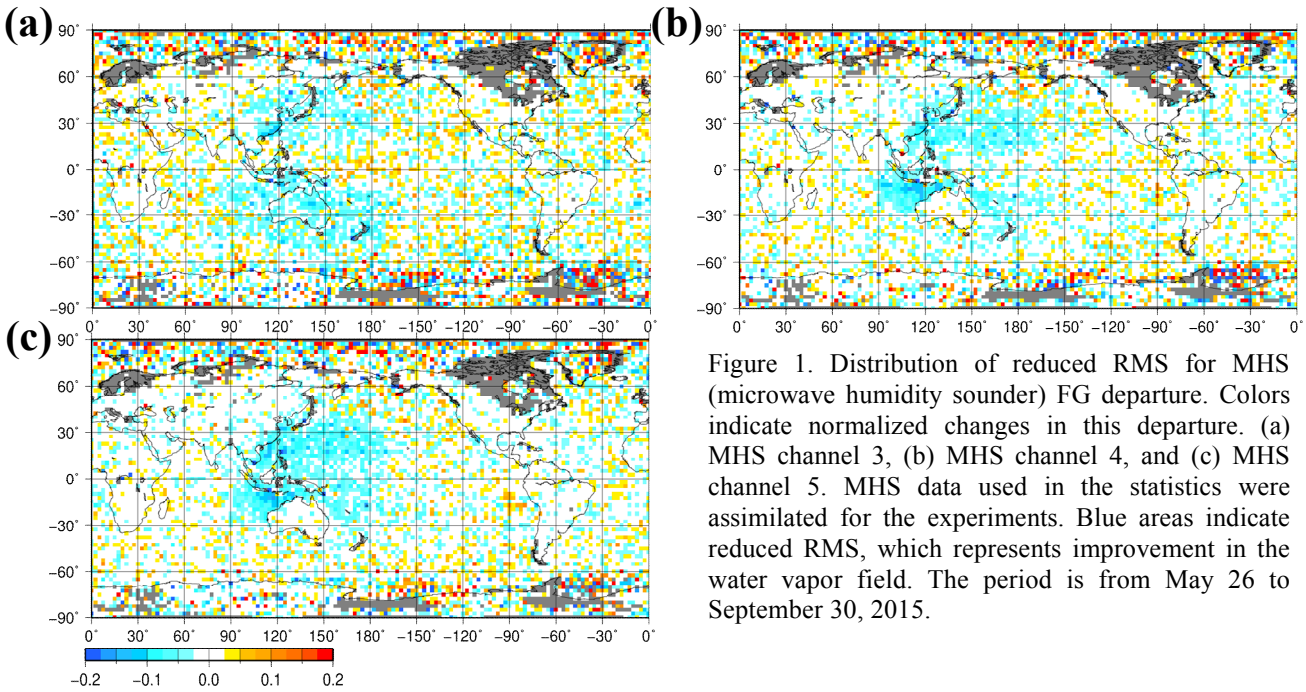

Figure 1. Distribution of reduced RMS for MHS (microwave humidity sounder) FG departure. Colors indicate normalized changes in this departure. (a) MHS channel 3, (b) MHS channel 4, and (c) MHS channel 5. MHS data used in the statistics were assimilated for the experiments. Blue areas indicate reduced RMS, which represents improvement in the water vapor field. The period is from May 26 to September 30, 2015.

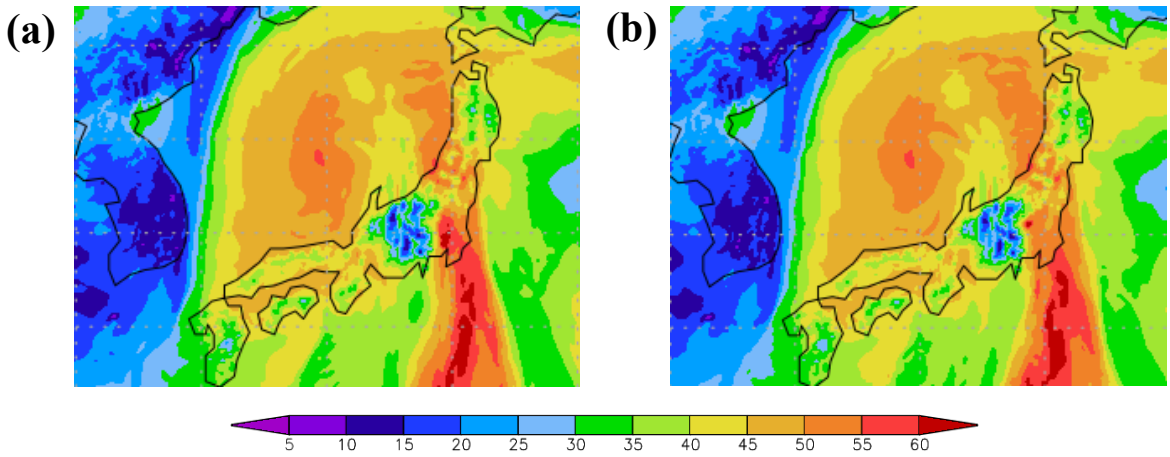

Figure 2. Comparison of analyzed total column water vapor between (a) Himawari-8 CSR usage and (b) MTSAT-2 CSR usage. The analysis time is 12 UTC on September 9, 2015, and the unit is mm.

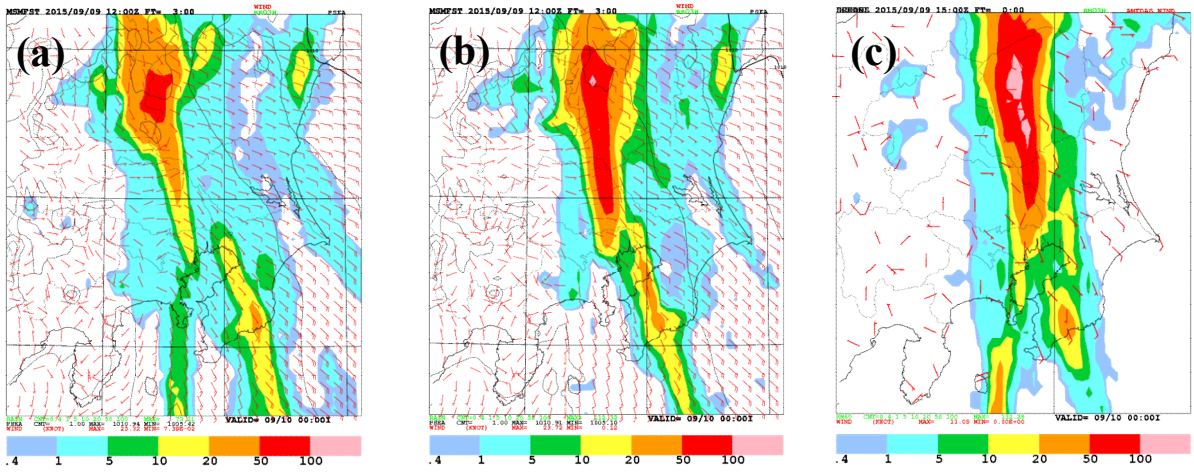

Figure 3. Comparison of three-hour cumulative rainfall forecasts for 15 UTC on September 9, 2015. The forecast period is three hours. Panel (a) shows the results without Himawari-8 CSR, panel (b) shows those with Himawari-8 CSR, and panel (c) shows rainfall distribution estimated from radar observations and rain gauges. The unit is mm/3 hrs.

Assimilation of Megha-Tropiques/SAPHIR radiance data in JMA's global NWP system

Masahiro Kazumori
Numerical Prediction Division, Forecast Department, Japan Meteorological Agency
Corresponding author: M. Kazumori, JMA, Otemachi, Chiyoda-ku, Tokyo, 100-8122, Japan
E-mail: kazumori@met.kishou.go.jp

Introduction

Space-based microwave radiance observation data are an essential part of accurate water vapor analysis for numerical weather prediction (NWP). Such data provide information on atmospheric water vapor in clear sky conditions, and their assimilation can be expected to improve initial fields for NWP. In this context, a joint mission of the Indian Space Research Organization (ISRO) and the Centre National d'Etudes Spatiales (CNES) launched the Megha-Tropiques satellite into a low-inclination orbit to observe tropical regions. The satellite carries a microwave humidity sounder (SAPHIR) with six 183 GHz water vapor absorption channels. Since the limitation of the satellite's orbit in tropical regions allows for frequent observation of these areas, the resulting data reflect rapidly changing water vapor profiles associated with tropical meteorological phenomena. As a result, assimilation of these data is expected to improve water vapor analysis and tropical cyclone prediction. The data have been available in real time to the NWP community since 2014, and related assimilation experiments have been conducted in JMA's global NWP system.

Methodology

Satellite radiance assimilation in JMA's global NWP system currently uses clear-sky radiance data. Accordingly, a cloud screening method for SAPHIR radiance data needed to be developed to enable the selection of clear-sky data for assimilation. As no window channel is available for SAPHIR, the relationship between the observed and simulated radiances of the channels adjacent to the one for assimilation were examined, and the empirical cloud detection thresholds of the difference between estimated clear-sky radiance and observed radiance were determined. This empirical cloud detection method is effective in screening out cloud-affected SAPHIR radiances in preprocess of the assimilation. SAPHIR land data are also removed to avoid surface signal contamination under dry atmospheric conditions. RTTOV version 10 was used as the radiative transfer model for assimilation.

Assimilation Experiments

Assimilation experiments for clear-sky SAPHIR radiance data were conducted with JMA's global NWP system for July, August, September and December of 2014, and for January and February of 2015. Assimilation brought significant improvements in analyzed water vapor fields and first-guess (FG) departure fits to other humidity and temperature observations. These changes (i.e., reduction of the FG departure's standard deviation) were statistically significant, and all results indicated consistent improvement of water vapor fields in analysis and FG (Figure 1). The improvements were dominant for the tropics. Assimilation of SAPHIR radiance data also significantly improved tropical cyclone track prediction in the JMA system for the experiment period (Figure 2).

Summary

Assimilation of SAPHIR radiance data in JMA's global NWP system improved water vapor analysis and FG fields. From FG fits to radiosonde observations and other humidity-sensitive satellite radiance data in the tropics, both water vapor profiles and column water vapor amounts were considered to be improved in analysis and FG. Small improvements of AMSU-A channel 4 to 6 indicate the amelioration of lower-tropospheric temperatures in the tropics. These improvements represent a promising contribution to better tropical cyclone analysis and prediction. Based on these

findings, assimilation of SAPHIR radiance data into JMA's global NWP system was begun in June 2015.

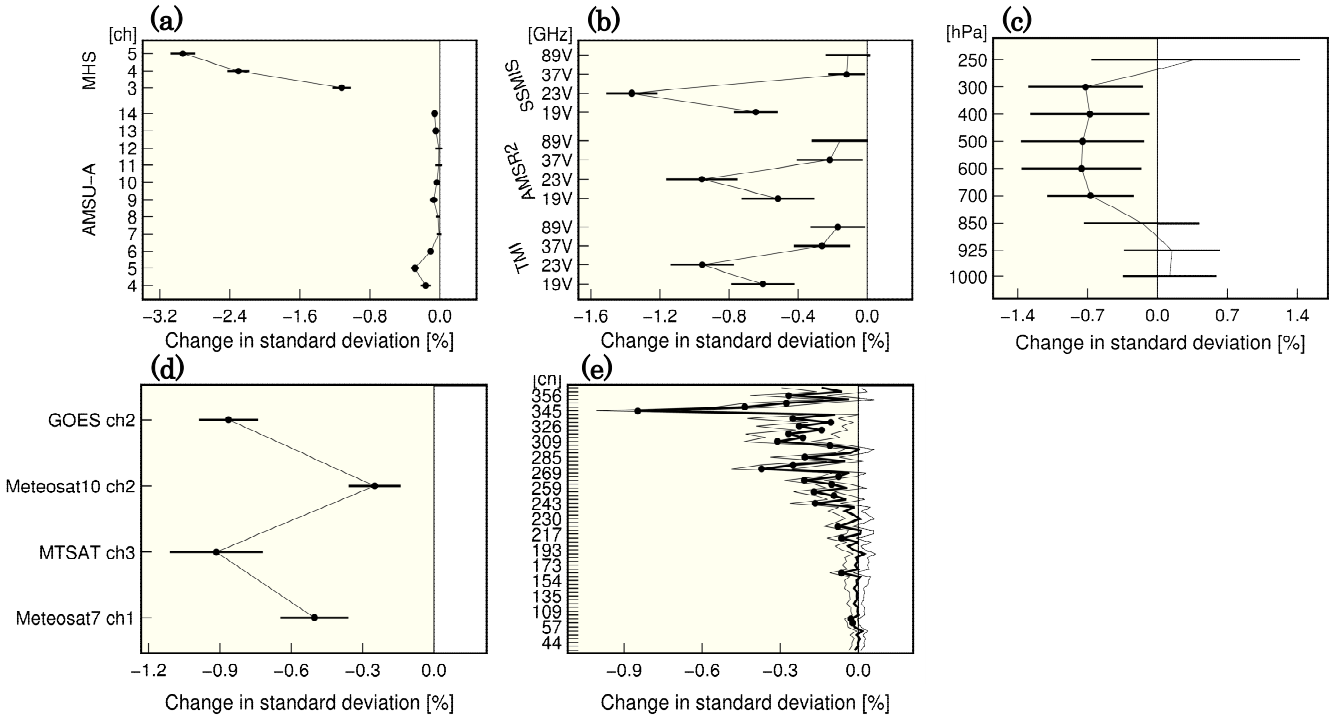

Figure 1. Normalized difference of standard deviation [%] in FG departure for (a) AMSU-A and MHS, (b) microwave imagers, (c) radiosonde relative humidity observation, (c) clear sky radiance (CSR) from geostationary satellites, and (e) IASI channels in the tropics. Negative values correspond to reduced standard deviation with SAPHIR radiance assimilation. Black dots indicate statistical significance, and error bars show a 95% confidence interval.

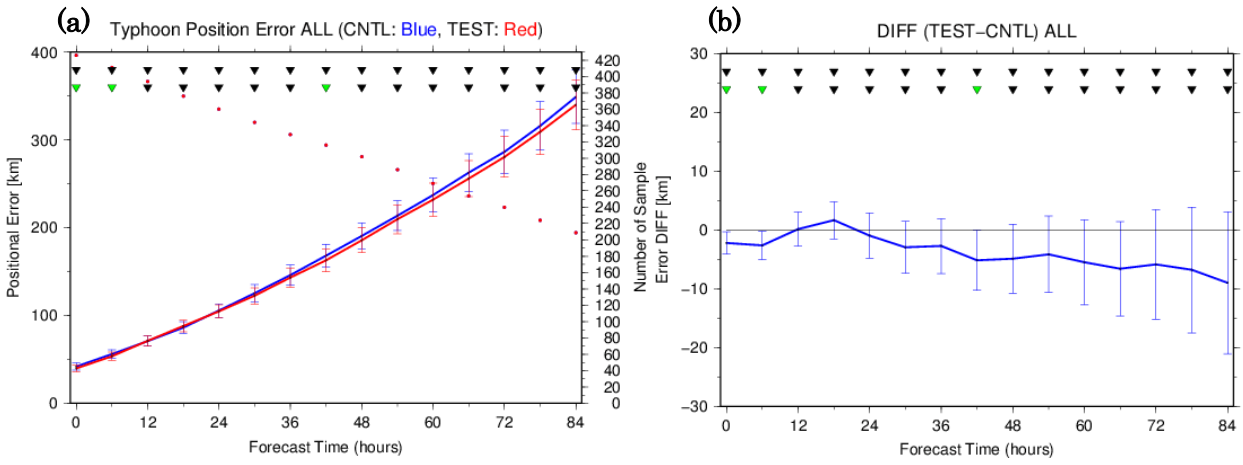

Figure 2. (a) Average typhoon track forecast errors for July, August, September and December 2014, and for January and February 2015. The red and blue lines represent the positional errors of TEST (with SAPHIR) and CNTL (without SAPHIR), respectively. Red dots indicate the number of cases included in the statistics. The error bars represent a 95% confidence interval. Best track data as truth are taken from RSMC Tokyo – Typhoon center analysis. The horizontal axis indicates the forecast time. (b) Typhoon position error difference between TEST and CNTL. The green triangles at the top in both panels indicate statistical significance in the difference. Negative values indicate error reduction.

Stochastic ensemble Kalman filter with ensemble generation using a square root form: ensemble π-algorithm

Ekaterina Klimova

Institute of Computational Technologies SB RAS,

Ac. Lavrentjev Ave., 6, Novosibirsk, 630090, Russia

klimova@ict.nsc.ru

1. Introduction

The Kalman filter algorithm is one of the most popular approaches to observation data assimilation. To implement the ensemble algorithm, the number of ensemble members must not be too large. Also, the ensemble must have a covariance matrix consistent with the covariances of analysis errors. There exist two approaches to the ensemble Kalman filter: a "stochastic filter" and a "deterministic filter". A large body of research has been made to compare stochastic and deterministic filters. As shown in several studies, the stochastic ensemble Kalman filter has advantages over a deterministic filter.

In [6], a stochastic version of the ensemble Kalman filter, which is implemented in the square root form (the ensemble π-algorithm) is proposed. The ensemble π–algorithm is what is called a stochastic filter in which an ensemble of analysis errors is generated by transforming an ensemble of forecast errors using a square root form. The transformation matrix does not depend on grid nodes. Therefore, the algorithm can be used locally, in a similar way as the LETKF algorithm [4] and can be implemented involving operations with matrices of size not greater than that of the ensemble.

A new numerical implementation scheme of the ensemble π-algorithm is proposed. In particular, we consider a more general approach than that proposed in [6] to calculate the square root of a non-symmetric matrix. Our approach is compared with the classical stochastic Kalman filter [2, 3] on the test example. The comparison showed the efficiency of proposed algorithm.

2. Ensemble π -algorithm

The ensemble π-algorithm is a stochastic filter. In this algorithm the analysis step is carried out only for the ensemble mean. The ensemble of analysis errors $\mathbf{D}$ is a matrix of dimension $(L \times N)$ which columns are vectors $\{\mathbf{dx}_k^n, n = 1,\ldots,N\}$, where $\mathbf{dx}_k^n \triangleq \mathbf{x}_k^{a,n} - \overline{\mathbf{x}_k^{a,n}}$, k is the number of time step, n is the ensemble number. It is obtained by transformation of the ensemble of forecast errors $\mathbf{F}$ - matrix with columns $\{\mathbf{f}_k^n, n = 1,\ldots,N\} : \mathbf{f}_k^n = \mathbf{x}_k^{f,n} - \overline{\mathbf{x}_k^{f,n}}$: $\mathbf{D}^{\mathrm{T}} = (\mathbf{I} + \mathbf{\Pi}^{\mathrm{T}})^{-1}\mathbf{F}^{\mathrm{T}}$, where

$$\mathbf{\Pi}^{\mathrm{T}} = (\mathbf{C} + 0,25\mathbf{I})^{\frac{1}{2}} - 0,5\mathbf{I}, \tag{1}$$

$$\mathbf{C} = \frac{1}{N-1}\mathbf{F}^{\mathrm{T}}\mathbf{H}^{\mathrm{T}}\mathbf{R}^{-1}(\mathbf{HF} + \mathbf{E}) = \mathbf{C}_1 + \mathbf{C}_2. \tag{2}$$

$\mathbf{E}$ is a matrix whose columns are the vectors $\boldsymbol{\varepsilon}_k^n$ - the ensemble of observational errors. More detailed description is presented in [6].

Elements of matrix $\mathbf{\Pi}$ are calculated for the ensemble $\{\mathbf{dx}_k^n, n = 1,\ldots,N\}$, the matrix $\mathbf{H}$ and matrix $\mathbf{R}$ do not depend on the grid node. This makes it possible to implement the algorithm

locally. At the same time the implementation of the ensemble π-algorithm requires operations with matrices whose dimension is equal to the ensemble dimension. Note that the above properties are typical of the popular LETKF algorithm [4], which is a deterministic filter.

3. Practical implementation of the ensemble π-algorithm

For implementation of the algorithm the solution of equation (1) is required, i.e. the calculation of the square root of the matrix $(\mathbf{C}+0,25\mathbf{I})$. In [6] an approximate estimate of the square root of the matrix $(\mathbf{C}+0,25\mathbf{I})$ is proposed. Let us consider a more general approach. As can be seen from formula (2), this matrix is non-symmetric. To calculate the square root of the matrix the algorithm proposed in [1] can be applied. This algorithm is based on the Schur triangular decomposition. It can be shown that the real part of the eigenvalues of the matrix $(\mathbf{C}+0,25\mathbf{I})$ is positive and the algorithm proposed in [1] can be applied to calculate the square root of this matrix.

For calculation of the inverse matrix $(\mathbf{I}+\mathbf{\Pi}^{\mathrm{T}})^{-1}$ the symmetrization using the multiplying by the transposed matrix was performed: $(\mathbf{I}+\mathbf{\Pi})(\mathbf{I}+\mathbf{\Pi}^{\mathrm{T}})\mathbf{D}^{T}=(\mathbf{I}+\mathbf{\Pi})\mathbf{F}^{T}$. To solve the resulting equation the eigenvalues and eigenvectors of a symmetric matrix were used.

There is no problem of zero eigenvalues arising during calculation of the inverse matrix in the π-algorithm. Thus, the singular value decomposition is not required as it is in the algorithm for stochastic ensemble Kalman filter proposed in [2, 3].

4. Conclusions

This article describes an efficient algorithm for data assimilation based on a stochastic ensemble Kalman filter - ensemble π-algorithm. A numerical method for the implementation of this algorithm is proposed. Numerical experiments conducted in three-dimensional domain with model data have shown the effectiveness of the ensemble π-algorithm, as compared with the algorithm of the stochastic Kalman filter proposed in [2, 3]. Root-mean-square error of analysis step of the ensemble π-algorithm in the model experiments is very close to the errors in the classical stochastic Kalman filter, and the gain in computer time becomes especially great while the number of observations used in the analyses increases.

References

1. Àke Björck, Sven Hammarling A Schur method for the square root of a matrix. Linear algebra and its applications. 52/53: 127-140. 1983
2. Evensen G. Sequential data assimilation with a nonlinear quasi-geostrophic model using Monte Carlo methods to forecast error statistics. Journal Geophysical Research. 1994. V.99. P.10143-10162.
3. Evensen G. Data assimilation. The ensemble Kalman filter. 2009. Spriger-Verlag: Berlin Heideberg 307 p.
4. Hunt B.R., Kostelich E.J., Szunyogh I. Efficient data assimilation for statiotemporal chaos: A local ensemble transform Kalman filter. Physica D. 2007. V.230. P.112-126.
5. Klimova, E. G. A Data Assimilation Technique Based on the pi-algorithm. Russian Meteorology and Hydrology. 2008. Volume 33. Issue 3. Pages 143-150. DOI: 10.3103/S1068373908030023.
6. Klimova E. A suboptimal data assimilation algorithm based on the ensemble Kalman filter. Quarterly Journal of the Royal Meteorological Society. 2012. V.138. P.2079-2085. DOI:10.1002/qj.1941.

Assimilation of surface pressure in METAR

Yuki Kosaka[1]
Numerical Prediction Division, Japan Meteorological Agency
E-mail: yuki-kosaka@met.kishou.go.jp

1. Introduction

Observation data reported in METAR format (e.g., those relating to pressure, temperature and wind) are useful information for NWP. The Japan Meteorological Agency (JMA) began assimilating surface pressure data in METAR into its global NWP system in October 2015. This report outlines the usage of surface pressure data in METAR and related impacts on the global NWP system.

2. Overview of METAR and quality control procedure for surface pressure data

Figure 1 shows the worldwide coverage of stations reporting METAR, which number around 4,000. Approximately half of these stations also report SYNOP or are collocated with SYNOP-reporting stations. METAR-reporting stations have a tendency of concentration in the USA (in contrast to the situation with SYNOP-reporting stations), but are also found on the African Continent and Pacific islands where SYNOP-reporting stations are scarce. Since METAR observation data provide valuable information from these areas, it is beneficial to improve the quality of analysis fields by assimilating observation data in METAR.

The METAR surface pressure data assimilated into JMA's global NWP system is QNH, which is defined as mean sea level pressure corrected using the ICAO (International Civil Aviation Organization) standard atmospheric profile. QNH is generally rounded down to the nearest whole hPa for METAR reports. In addition, stations in some countries (e.g., Japan, the USA and Canada) also report QNH in hundreds of inches of mercury with a precision of 0.01 inHg (approx. 0.3386 hPa).

The quality control (QC) procedure for surface pressure in METAR is based on Ingleby (2014). Since the reporting of QNH in hundreds of inches of mercury is more precise than that in whole hPa, such QNH reports are assimilated into the analysis prior to those in whole hPa. For QNH reports in whole hPa, which are rounded down for METAR reports, 0.5 hPa is added to avoid systematic errors. The Blacklist check, the climatological check, the inter-element consistency check, the gross error check and the spatial consistency check are applied for QC (see JMA (2013)). When observed surface pressure is assimilated, values generally need to be converted to model surface height equivalents for comparison with first-guess field variables. This is achieved by first converting QNH to station-level pressure using the ICAO standard atmospheric profile, then converting this to model surface height pressure using the atmospheric profile applicable at the time of observation.

Figure 2 shows histograms of the first-guess (FG) departure of pressure at model surface height. Normal distribution is seen for both METAR and SYNOP. The average and standard deviation of FG departure for METAR are similar to those for SYNOP. These results are consistent with those of Ingleby (2014), which showed that the quality of surface pressure data in METAR is comparable to that in SYNOP.

---

[1] Current affiliation: Climate Prediction Division, JMA

3. Impacts on the global NWP system

Observing system experiments were performed for the two months of August 2014 and January 2014 to evaluate the impacts of METAR assimilation. The control experiment (CNTL) had the same configuration as the operational global NWP system of September 2014, and surface pressure data in METAR were additionally assimilated in the test (TEST) experiment. Figure 3 shows the normalized difference (TEST-CNTL) of standard deviation in analysis (AN) departure for surface pressure in SYNOP. Standard deviation in AN departure for the TEST experiment was smaller than that for the CNTL experiment, indicating improved analysis field quality. Impacts on the forecast score were almost neutral.

References

Ingleby, B., 2014: Global assimilation of air temperature, humidity, wind and pressure from surface stations. *Quart. J. Roy. Meteor. Soc.*, doi: 10.1002/qj.2372

JMA, 2013: Data Assimilation Systems. *Outline of the operational numerical weather prediction at the Japan Meteorological Agency. Appendix to WMO Technical Progress Report on the Global Data-processing and Forecasting System,* Japan Meteorological Agency, Tokyo, Japan, 10-40.

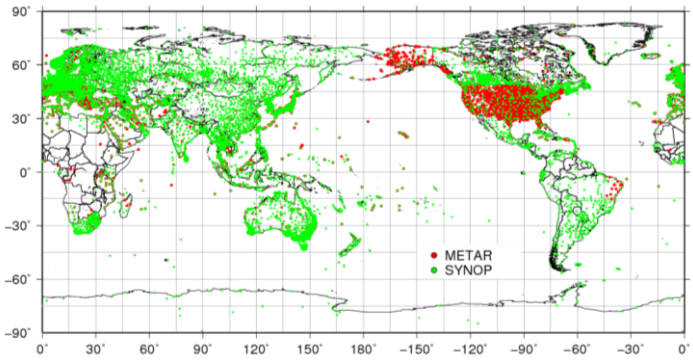

Figure 1: Stations reporting METAR (red dots) and SYNOP (green dots)

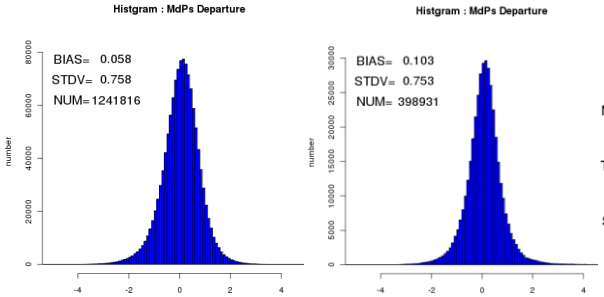

Figure 2: Histograms of FG departure [hPa] for pressure at model surface height
Left: METAR; right: SYNOP

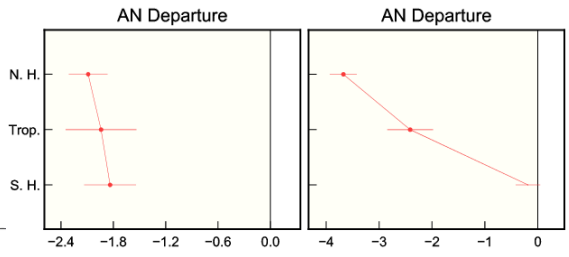

Figure 3: Normalized difference (TEST – CNTL [%]) of standard deviation in AN departure for surface pressure in SYNOP. N.H., Trop and S.H. indicate the Northern Hemisphere, the tropics and the Southern Hemisphere, respectively. Red dots indicate a statistically significant difference.
Left: Aug. 2014; right: Jan. 2014

Operational use of ASCAT ocean vector wind data in JMA's mesoscale NWP system

Masami Moriya
Numerical Prediction Division, Japan Meteorological Agency
E-mail: m.moriya@met.kishou.go.jp

1. Introduction

Assimilation of scatterometer ocean vector wind (OVW) data is expected to improve lower-level initial wind fields for weather forecasting, as confirmed by JMA's use of ASCAT (-A and -B) OVW data in its global NWP system since July 2009 (Takahashi 2010, Moriya 2014). In December 2015, JMA began operational utilization of ASCAT OVW data in its mesoscale NWP system after results from observing system experiments (OSEs) had indicated related improvements in analysis and forecast fields. This report outlines the impact of ASCAT OVW data on JMA's mesoscale NWP system.

2. Data quality investigation

A data quality investigation was conducted by means of first-guess departure (observation – background) statistics using the whole data set for 2014. The results showed that the first-guess departure largely followed Gaussian distribution with a mean error of 0.14 m/s and a standard deviation of 1.4 m/s, which are comparable to the corresponding figures for the global NWP system.

3. Verification results

OSEs were performed using JMA's mesoscale NWP system for individual periods of approximately a month for winter 2014 and summer 2014 to determine the impacts of ASCAT OVW data. The control experiment (CNTL) had the same configuration as the operational system, and the test experiment (TEST) was exactly the same as CNTL except for the additional use of ASCAT OVW data.

Figure 1 shows the normalized difference of standard deviation (STDV) for the first-guess departure of wind speed with regard to several wind observations used as baselines. STDV is reduced in particular at lower levels, indicating that the difference in the first-guess wind field and observational data decreases with assimilation of ASCAT OVW data. Similar results were also found for other elements such as mean sea level pressure and brightness temperature from satellite observation.

Figures 2 and 3 show precipitation forecast scores. The equitable threat score for heavy rain (40 mm/3 hours) in the summer experiment and moderate rain (10 and 30 mm/3 hours) in the winter experiment improved, while no particular improvement was observed in the bias score for either experiment.

The benefits of ASCAT OVW data utilization in JMA's mesoscale system were thus identified, and JMA began operational assimilation of the data in December 2015.

References

Takahashi, M., 2010: Operational use of Metop-A/ASCAT Winds in the JMA Global Data Assimilation System. *CAS/JSC WGNE Res. Activ. Atmos. Oceanic Modell.*, **40**, 01.39-01.40.

Moriya, M., 2014: Utilization of Metop-B data in JMA's Operational Global and Mesoscale NWP Systems. *CAS/JSC WGNE Res. Activ. Atmos. Oceanic Modell.*, **44**, 01.13-01.14.

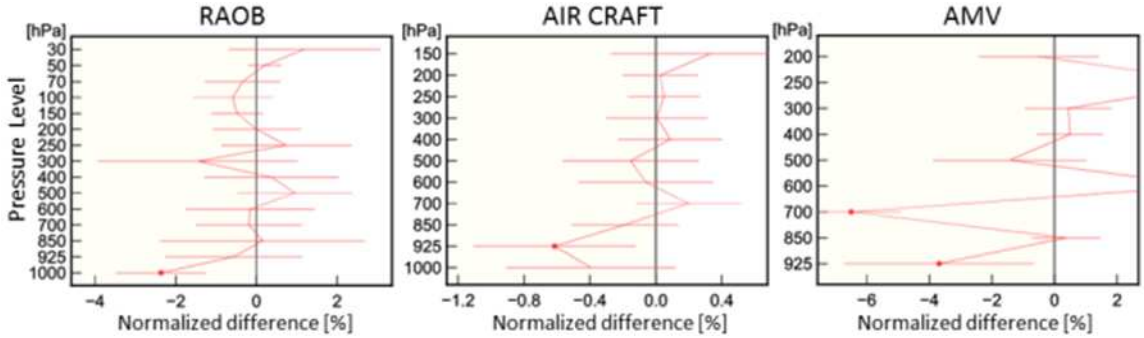

Figure 1: Normalized difference of STDV for the first-guess departure of wind speed ($(STDV_{TEST} - STDV_{CNTL}) / STDV_{CNTL}$) with regard to rawinsonde (RAOB) observation, aircraft observation and AMVs in the January 2014 experiment. Negative values represent improvement. The horizontal axis indicates normalized STDV difference and the vertical axis indicates vertical levels. The error bars represent a 95% confidence interval, and the red dots represent statistically significant values.

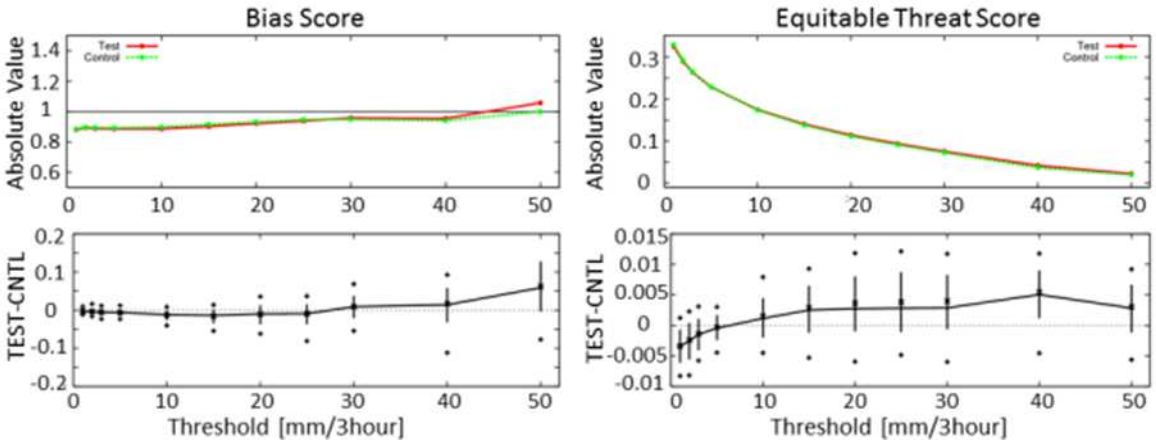

Figure 2: Precipitation forecast scores in the July 2014 experiment. The top figures show absolute bias scores (left) and equitable threat scores (right). The red and green lines represent TEST and CNTL, respectively. The bottom figures show TEST – CNTL for the bias score (left) and the equitable threat score (right). The error bars represent a 95% confidence interval, and the two dots at each threshold represent the max./min. difference.

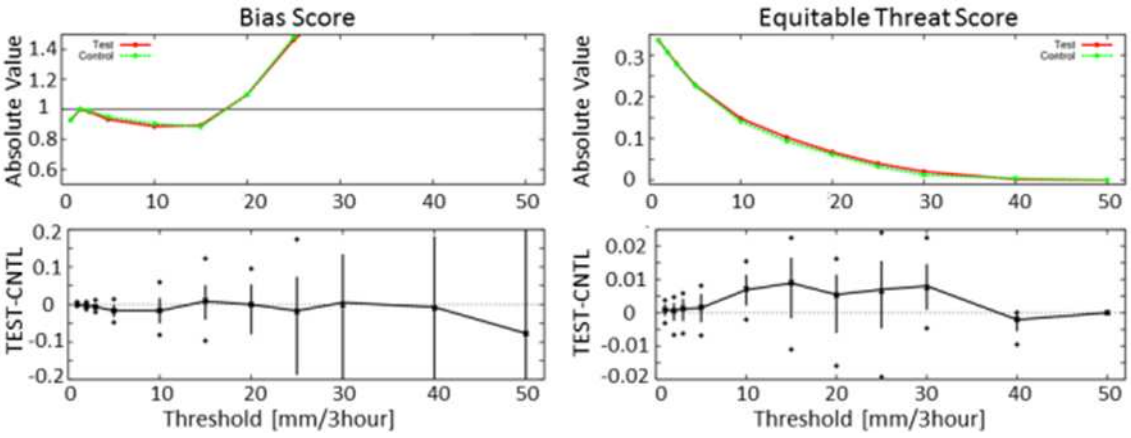

Figure 3: As per Fig. 2 but for January 2014

Development Progress on the Real Time Mesoscale Analysis (RTMA) and UnRestricted Mesoscale Analysis (URMA) Systems at NCEP/EMC

Manuel Pondeca[a], Steven Levine[b], Runhua Yang[a], Annette Gibbs[a], Jacob Carley[a], Geoff Manikin[c], Corey Gaustini[a], Ying Lin[c], Jim Purser[a], Xiujuan Su[a], Jeff Whiting[a], Dave Parrish[c], Geoff DiMego[c]
[a]*IM Systems Group Rockville, MD* [b]*Systems Research Group Colorado Springs, CO*
[c]NOAA/NWS/NCEP/EMC College Park, MD

NCEP's Real Time Mesoscale Analysis System (RTMA) is designed to provide the highest quality real time gridded surface analysis for National Weather Service operations [1]. The UnRestricted Mesoscale Analysis is run 6 hours later, which allows for the use of latent observational data and is designed to be used for verification and/or tuning, such as with the National Blend of Models project [2]. In addition to the substantial changes introduced in the system last year, additional improvements are being made to the system, with the help of forecaster feedback. New analysis variables are being added to support URMA's role as the 'analysis of record' for the National Blend of Models project on grids matching those of the National Digital Forecast Database.

Quality Control Improvements

Surface observations (including mesonet observations) are heavily used in the RTMA/URMA, and quality control of these observations is critical since many are not necessarily sited or maintained at the same level as ASOS or AWOS sites. Variational quality control has been introduced to help with this. The variational quality control is designed to alter the weight given to a particular observation based on its match to the background field and neighboring observations. The variational quality control was implemented for temperature, moisture and pressure observations in January 2016. Its use has been shown to reduce the intensity of 'bulls-eyes' that often occur around isolated observations significantly different than the background.

New Variables

At the request of the National Blend of Models project, a minimum and maximum temperature analysis was added to URMA. One minT analysis and one maxT analysis is run daily for each domain. The analysis selects the highest (lowest) background field value for each point and the highest (lowest) observed value for each temperature observation at each observation site (mobile sites and sites that do not report regularly are not considered) over the time period for maximum (minimum) temperature as defined in the National Digital Forecast Database: 7A-7P LST for maximum temperature and 7P-8A LST for minimum temperature. Min/maxT was implemented for CONUS and Alaska in January 2016 and will be implemented for Hawaii and Puerto Rico in mid-2016.

A ceiling analysis is also being added to the system. The system uses ceiling observations derived from METAR observations and a RAP/HRRR-based background field. Ceiling is being added to support that National Blend of Models project and also at the request of the FAA and NWS/AWC. Towards the end of 2016, we intend to begin running a 15-minute rapidly updating analysis of ceiling and visibility to support FAA and AWC.

Recent feedback from the field has indicated that the RTMA/URMA system's wind analysis does not closely match available observations and often shows wind features which are not physically consistent with local terrain or conditions. RTMA/URMA has thus far not analyzed wind itself, but rather stream function and velocity potential which is converted to and from wind speed and direction. In an attempt to correct the issues seen by field forecasters, wind speed is now being analyzed as a scalar. Wind direction will still be derived from the stream function and velocity potential analysis. The new wind speed analysis ensures that wind speed increments are consistent with available observations and therefore provide a closer match to those observations.

Field Feedback

Since the RTMA/URMA is used as an analysis of record for verification and grid initialization locally and nationally, feedback from field users is critical in furthering development of the system [3]. The wind speed scalar analysis was added at the specific request of users from NWS local and regional offices, for example. An email listserver (aor-rtma@infolist.nws.noaa.gov) and a NOAA Virtual Lab community (https://vlab.ncep.noaa.gov/group/715073/home) are used to gather and facilitate feedback and to give updates to the user community on development progress. The developers welcome any feedback or suggestions on improving the analysis; both the listserv and VLab community are open to people both inside and outside of NOAA. A NOAA-only website has also been developed to allow forecasters to compare operational and development versions of URMA against NDFD grids and other analysis schemes such as BDCG and LAPS.

References

[1] Manuel S. F. V. De Pondeca, Geoffrey S. Manikin, Geoff DiMego, Stanley G. Benjamin, David F. Parrish, R. James Purser, Wan-Shu Wu, John D. Horel, David T. Myrick, Ying Lin, Robert M. Aune, Dennis Keyser, Brad Colman, Greg Mann, and Jamie Vavra, 2011: The Real-Time Mesoscale Analysis at NOAA's National Centers for Environmental Prediction: Current Status and Development. Wea. Forecasting, 26, 593–612. doi: http://dx.doi.org/10.1175/WAF-D-10-05037.1

[2] K. K. Gilbert, J. P. Craven, D. R. Novak, T. M. Hamill, J. Sieveking, D. P. Ruth, and S. J. Lord, 2015: An Introduction to the National Blend of global Models Project. Special Symposium on Model Postprocessing and Downscaling, Phoenix, AZ, Amer. Meteor. Soc., 3.1.

[3] Levine, S., M.Pondeca, J. Carley, Y. Lin, R. Yang, A.M. Gibbs, Y. Zhu, R.J. Purser, D.F. Parrish, D. Myrick, J. McQueen, D. Radell, and G. DiMego, 2015: The Continued Improvement of NCEP's RTMA/URMA System and Benefits of Field Interaction toward the 2015 operational upgrades. Preprints, 27th Conference On Weather Analysis And Forecasting/23rd Conference On Numerical Weather Prediction, Amer. Meteor. Soc., 6A.6. [Available online at: https://ams.confex.com/ams/27WAF23NWP/webprogram/Paper273607.html**]**

Assimilation of JMA high-resolution radiosonde observation data into the mesoscale 4D-Var data assimilation system

Hiroshi Sako
Office of Observation Systems Operation, Japan Meteorological Agency
E-mail: h-sakou@met.kishou.go.jp

Introduction

In recent years, the Japan Meteorological Agency (JMA) has introduced GPS radiosondes for all its radiosonde stations. Conventional TEMP bulletins contain observation values for standard-pressure levels and significant levels but no positional information on radiosondes, which drift with the wind. However, the technological introduction of GPS radiosondes enables atmospheric observation at intervals of a few seconds (i.e., at several thousand altitudes in total) along with collection of positional information and storage of the results in high-resolution data (HRD) format. The assimilation of HRD with positional information is expected to improve the quality of initial atmospheric conditions and forecast accuracy. In consideration of such assimilation, JMA developed a new algorithm for quality control and data selection and evaluated the related impacts on forecasts using its mesoscale numerical weather prediction (NWP) system. The results showed that forecasts of precipitation and surface meteorological variables were improved by the use of HRD. Consequently, JMA began to assimilate HRD in its mesoscale NWP system in March 2016 using the new algorithm.

Quality control and data selection

The quality of HRD requires stringent control because greater amounts of data are more likely to be affected by measurement sensor problems and other issues. The quality control approach adopted for this purpose involves evaluation to determine the appropriateness of observation values and positions (i.e., whether temporal changes in observation values are rational). In addition, JMA's mesoscale 4D-Var data assimilation system is operated on the assumption of a no-error-correlation among observation data used in the process. Accordingly, HRD are thinned out with appropriate height intervals by following time displacements of around 60 seconds for temperature and dew point temperature, around 120 seconds for winds at levels lower than 850 hPa, around 120 seconds at levels from 850 through 200 hPa and around 240 seconds at levels higher than 200 hPa for all elements.

Impact of HRD on forecasts

Observing system experiments were performed for two months in summer 2015 and in winter 2014 – 2015 to evaluate the impact of JMA's HRD in its mesoscale NWP system. Forecasts with a lead time of 39 hours produced using JMA's mesoscale model (MSM) were run from each corresponding mesoscale analysis. In test runs, HRD were checked with the above-mentioned algorithm and selected data were assimilated at observed vertical and horizontal positions.

The equitable threat scores (ETSs) of three-hourly cumulative precipitation forecasts indicate that the quantitative precipitation forecasts of the test run were better than those of the control run for most precipitation thresholds in summer, while the impacts in winter were rather neutral (Fig. 1). A slight reduction of root mean square errors was seen in forecasts of

variables such as surface temperature and surface wind (in summer) and sea-level pressure (in both summer and winter) (Fig. 2). Figure 3 shows an example of improved precipitation forecasting. A strong rain band was observed in the area enclosed with the dashed blue line (c), and was found to be accurately forecast in the test run.

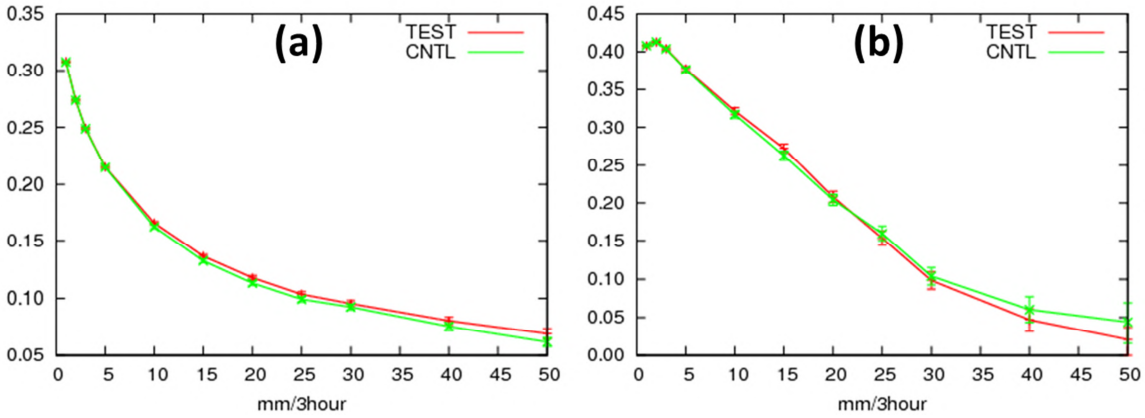

Fig. 1 Equitable threat scores (ETSs) of three-hourly cumulative precipitation in MSM forecasts against radar-raingauge analyzed precipitation: (a) summer experiment, (b) winter experiment. The scores of the test runs (TEST) are indicated by the red line, while those of the control runs (CNTL) are indicated by the green line, with error bars showing a 95% confidence interval.

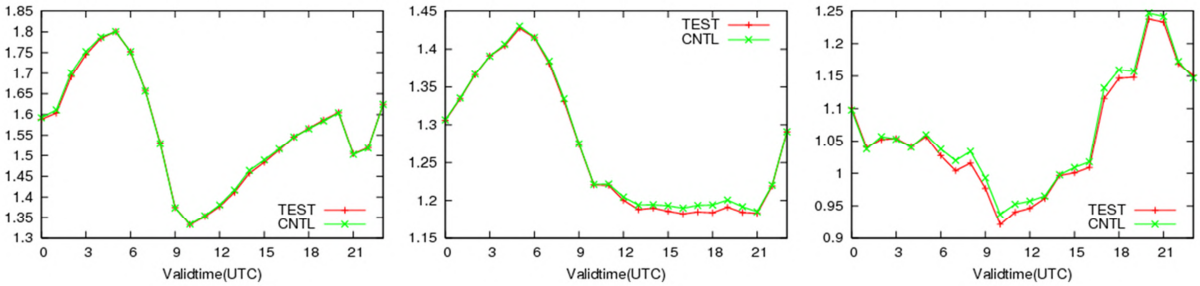

Fig. 2 Root mean square errors of surface temperature (left), surface wind velocity (middle), and sea-level pressure (right) in summer. The results of test runs (TEST) and control runs (CNTL) are shown in red and green, respectively. The horizontal axes indicate the forecast valid time (UTC).

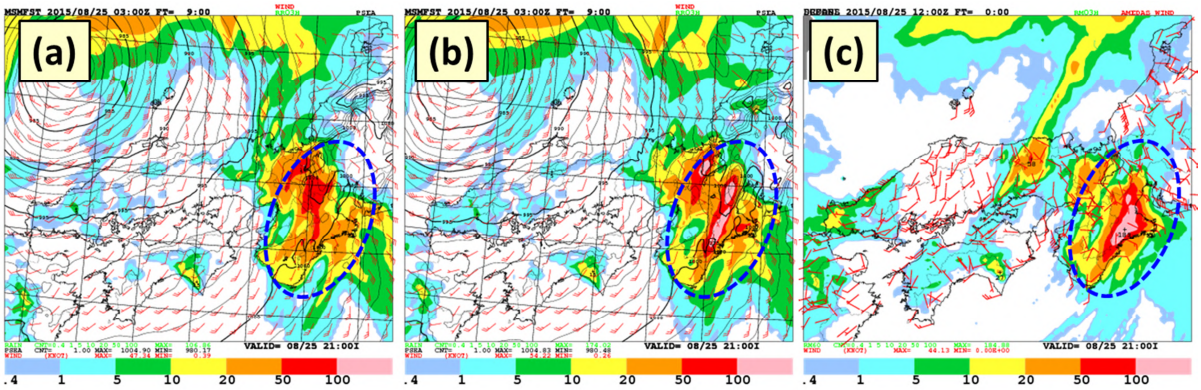

Fig. 3 Three-hourly cumulative precipitation at the forecast lead time of nine hours: (a) control run, (b) test run, and (c) observation

Data assimilation experiment of SSR mode-s downlink data

Hiromu Seko (MRI/JMA), Takayuki Yoshihara, and Atsushi Senoguchi (ENRI)
e-mail: hseko@mri-jma.go.jp

1. Introduction

New air control radars provide the high-frequent data (4-10 seconds) of horizontal wind and temperature, as well as the positions of airplanes. This data, which is known as SSR mode-s downlink data (hereinafter referred to as downlink data), is expected as assimilation data of operational numerical prediction systems. In this study, the impact of downlink data on a heavy rainfall that occurred in the Kanto region, Japan on 26th August 2011 was investigated with the data assimilation systems by using a Local Transform Ensemble Kalman Filter (LETKF).

The data assimilation experiment shows that the low-level convergence that caused the heavy rainfall was intensified by the downlink data and that the reproduced distribution of rainfall regions became similar to the observed one. This result indicates that the downlink data has potential to improve rainfall forecasts.

2. SSR mode-s downlink data

The information of airplanes (downlink data) as well as their positions was obtained by new air control radars (SSR mode-s) by inquiring each airplane individually from the radar. The downlink data includes the heading direction of airplanes, speeds relative to the ground and to the airflow, magnetic headings, and Mach numbers, from which the horizontal wind and temperature can be obtained.

The downlink data observed by air control radar of the Electronic Navigation Research Institute (ENRI, Koganei, Tokyo) was used in this study. The temporal interval of the data is 10 seconds. In addition to this frequency, many airplanes arrived at and departed from Haneda and Narita International Airports. The temporally and spatially dense profiles of horizontal wind and temperature around the airports were obtained by high-frequently requesting the responses from many airplanes. Figure 1 shows the spatial and temporal distribution of downlink data of 26th August. The temporal distribution indicates that the frequency of downlink data is high, except the midnight (from 00 LT to 06 LT).

It is known that the moderate vertical wind shear causes long-lasting convection systems, because the vertical wind shear shifts the position of downdraft from that of updraft. Therefore, the vertical profiles of horizontal wind are expected to be the important assimilation data that affect the duration and intensity of the convection systems.

3. Heavy rainfall event

A heavy rainfall event that occurred in the southern part of the Kanto Plain on the 26th of August 2011 was focused on as an object of data assimilation experiment. Intense rainfall regions were generated at mountainous areas of Japan and over the Kanto Plain (Fig. 3a). The intense rainfall regions over the Kanto Plain (indicated by a red rectangle in Fig. 3a) were generated around the convergence line of the southerly flow from the south and of the easterly flow that entered from the north-eastern side of the Kanto Plain (not shown). This airflow pattern is one of the popular ones when the heavy rainfalls occurred in the

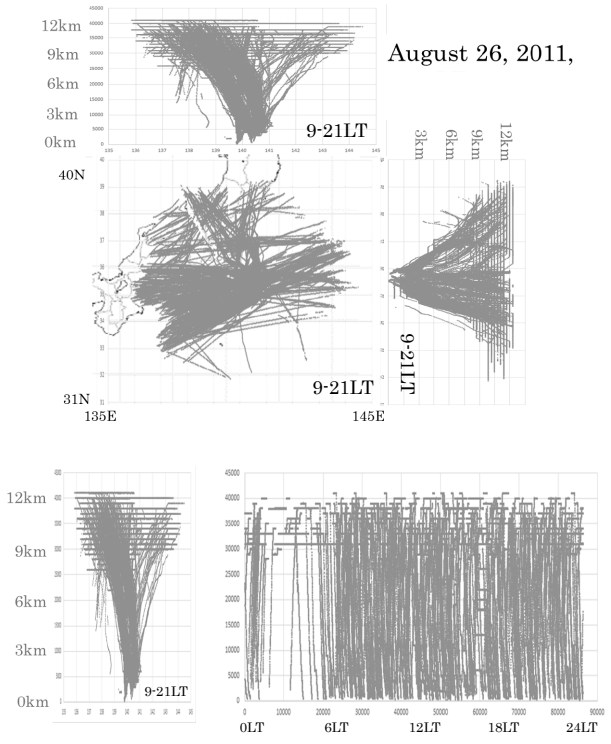

Fig. 1 Distributions of downlink data.

Kanto Plain in summer.

4. Data assimilation experiments

The temperature and horizontal wind that were used in this study were obtained in accordance with Shigetomi et al. (2013). The difference histogram of the observed horizontal wind and first-guess was shown in Fig. 2. There is a bias in the histogram of easterly wind, because the histogram was produced by only one day's data. Because this histogram looks like normal distribution, the horizontal wind from 09 LT to 15 LT (just before the occurrence of heavy rainfall) was used as assimilation data.

Data assimilation experiment was conducted by using the LETKF data assimilation system. The horizontal grid interval was 15 km. Data assimilation using a part of the Japan Meteorological Agency's conventional data started at 09 LT, 24, and downlink data was added to the assimilation data of 09 LT to 15 LT, 26.

Preliminary results of the data assimilation is shown in Fig. 3. When the downlink data was assimilated, the horizontal wind speed from the east at the height of 500 m became larger, and the convergence was intensified. Then, the rainfall distribution became similar to the observed one.

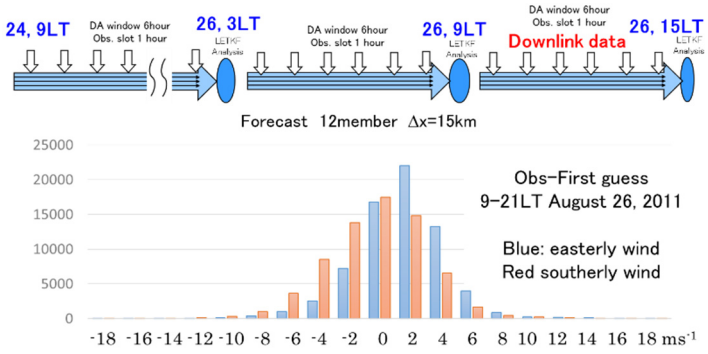

Fig. 2 Schematic illustration of assimilation experiment and difference between observation and first-guess of horizontal wind.

5. Summary

The downlink data obtained by air control radars provided the high-frequent vertical profiles of temperature and horizontal wind. Because the bias of horizontal wind that was observed on 26th August 2011 was a few meters, the downlink data was used as assimilation data. The reproduced rainfall distributions show that the downlink data made the rainfall region more similar to the observed one by modifying the horizontal wind fields. However, the observation error and the interval of data thinning were determined from one day's data. To further improve the rainfall forecasts, the observation error of downlink data and the optimal method of data thinning should be investigated. Further experiments are needed to obtain more conclusive results.

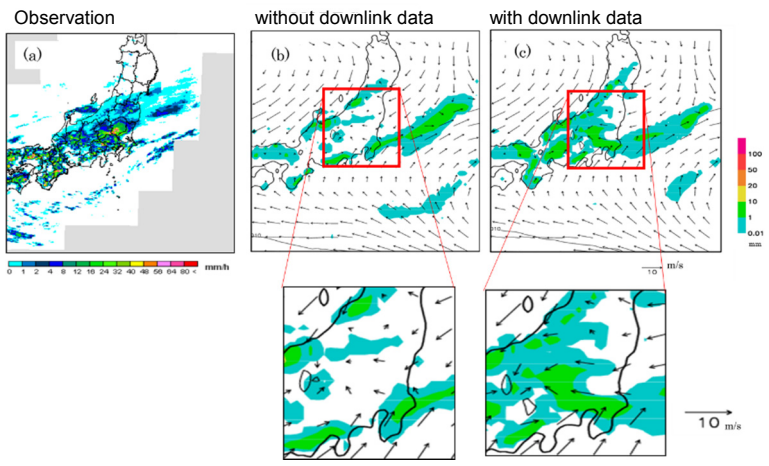

Fig. 3 Rainfall and horizontal wind distributions. (a) Observation, (b) and (c) the reproduced distributions obtained by assimilation of conventional data and downlink data. Height of horizontal wind is 500 m.

Reference:

Shigetomi et al., The evaluations and analyses of weather forecasts by using the SSR mode-s downlink data. The preprints of 51st airplane symposiums, JSASS-2013-5158 (In Japanese).

Acknowledgements:

This study was supported partly by the research project of "Tokyo Metropolitan Area Convection Study for Extreme Weather Resilient Cities (TOMACS)".

The Italian Air Force Met Service Operational NWP System

Lucio Torrisi and Francesca Marcucci
Italian Air Force Operational Centre for Meteorology (COMET), Italy
lucio.torrisi@am.difesa.it

The Italian Air Force Met Service short-range numerical weather prediction system is based on the Ensemble Kalman Filter (EnKF) approach [1,2] for the data assimilation component and the COSMO regional model (www.cosmo-model.org) for the prognostic one. In particular the Local Ensemble Transform Kalman Filter (LETKF [3]) scheme has been run operationally since June 2011.
The LETKF system makes use of a 40+1 member ensemble based on the COSMO model. The COSMO model is integrated on the European Mediterranean region at 10 km horizontal resolution on 45 model levels. A 6 hourly intermittent analysis cycle is implemented, making use of the observations available in a 6-h window centred at the analysis time. The observational dataset operationally ingested comprises drifting radiosonde ascents (4D-RAOB), surface pressure observations from land and sea stations (SYNOP, SHIP, BUOY), manual and automatic aircraft observations, atmospheric motion vectors from MSG3-MET7, European wind profilers, METOP scatterometer winds, NOAA and METOP AMSUA/MHS and NPP ATMS radiances. Assimilation of GPS Zenith Total Delay and MODE-S aircraft data is under testing.
Temperature, wind and specific humidity on model levels and surface pressure are provided as analysis fields. The deterministic COSMO-ME runs four times a day (00/06/12/18 UTC) with a 72h forecast range and 7 km resolution initialized by the LETKF control state analysis and driven by ECMWF forecasts. The very high-resolution COSMO-IT model is integrated over the Italian region (2.8km resolution), using COSMO-ME fields as boundary conditions. COSMO-IT is initialized by nudging scheme four times a day (00/06/12/18 UTC) and it is integrated up to 30 h. A schematic view of the operational NWP system is given in Fig.1.

LETKF Lateral Boundary Conditions Perturbation

Implementation of a limited-area ensemble Kalman filter (EnKF) needs a suitable way to perturb lateral boundary conditions. The ensemble of lateral boundary conditions is obtained perturbing the IFS deterministic forecast making use of the ECMWF-EPS. The 40 EPS members are randomly chosen and the perturbation of each one with respect to their mean is added to the most recent IFS deterministic forecast.
The Sea Surface Temperature (SST) is also climatologically perturbed using the differences of the IFS SST analysis from the ECMWF operational archive.

Model and sampling error treatment

A multiplicative and additive covariance inflation has introduced to ameliorate sampling errors due to small ensemble size and also to account for model errors in assimilating real observations.
The method proposed in [4], the so called "relaxation-to-prior spread" (RTPS), has been tested and implemented in the operational scheme, because the successful results with respect to other explored methods ("relaxation-to-prior perturbations" and "3-dimensional adaptive-temporally smoothed multiplicative inflation"). Because the RTPS is a purely multiplicative inflation method, a clear improvement is obtained when it is in combination with an additive inflation technique, designed in a way that it accounts for the flow dependency of the background covariance estimate.
The current operational implementation of the additive inflation uses the differences between ECMWF EPS ensemble forecasts valid at the analysis time interpolated on the COSMO grid. The mean difference is then removed to yield a set of perturbations that are globally scaled and used as additive noise.
Recently, an alternative adaptive flow-dependent additive inflaction has been implemented and experimentally tested. The perturbations are derived by a suitable scaling of the "zero-mean" differences of lagged LETKF ensemble forecasts giving a self-evolving and flow dependent additive noise. A small positive impact has been found at second day forecast, probably because this additive error has a component that projects onto the growing forecast structures. The use of SPPT (Stochastic Physics Perturbation Tendencies) in COSMO model has been also implemented.

The Italian Air Force Met Service Short Range Ensemble Prediction System: COSMO-ME EPS

The atmospheric short-range ensemble prediction system (COSMO-ME EPS) based on the LETKF analysis and the COSMO model is running operationally since July 2013.

The relevant characteristics of the atmospheric COSMO-ME EPS are:

- Domain and resolution: COSMO model is integrated 40 times on the same domain of the LETKF system.
- IC and BC: initial conditions are derived from the LETKF system; lateral boundaries conditions are from the most recent IFS deterministic run perturbed using ECMWF-EPS.
- Model error: stochastics physics perturbation tendencies.
- Forecast range: 72 hours at 00/12 UTC.

The Italian Air Force Met Service Operational Sea State Forecast System: NETTUNO

The NETTUNO [5] 3' system is based on the ECMWF version of WAM model integrated over the whole Mediterranean basin which is driven by COSMO-ME forecast winds. It was developed in cooperation with the ISMAR-CNR institute of Venice.

Forecast fields (mean wave period and direction, significant wave height) are given two times a day (00/12 UTC) every 3 hrs up to 72 hrs. A high resolution (1') WAM model driven by COSMO-IT wind forecast and nested in the 3' NETTUNO is integrated over the Italian domain.

A short range sea state EPS based on the NETTUNO system and the COSMO-ME EPS has been tested and implemented in collaboration with ISMAR-CNR.

The sea state probabilistic forecast is obtained driving the WAM model with the hourly COSMO-ME EPS wind forecast members. The NETTUNO-EPS consists of 40+1 members, that are integrated at 00 UTC up to 48 hour forecast in the Mediterranean basin.

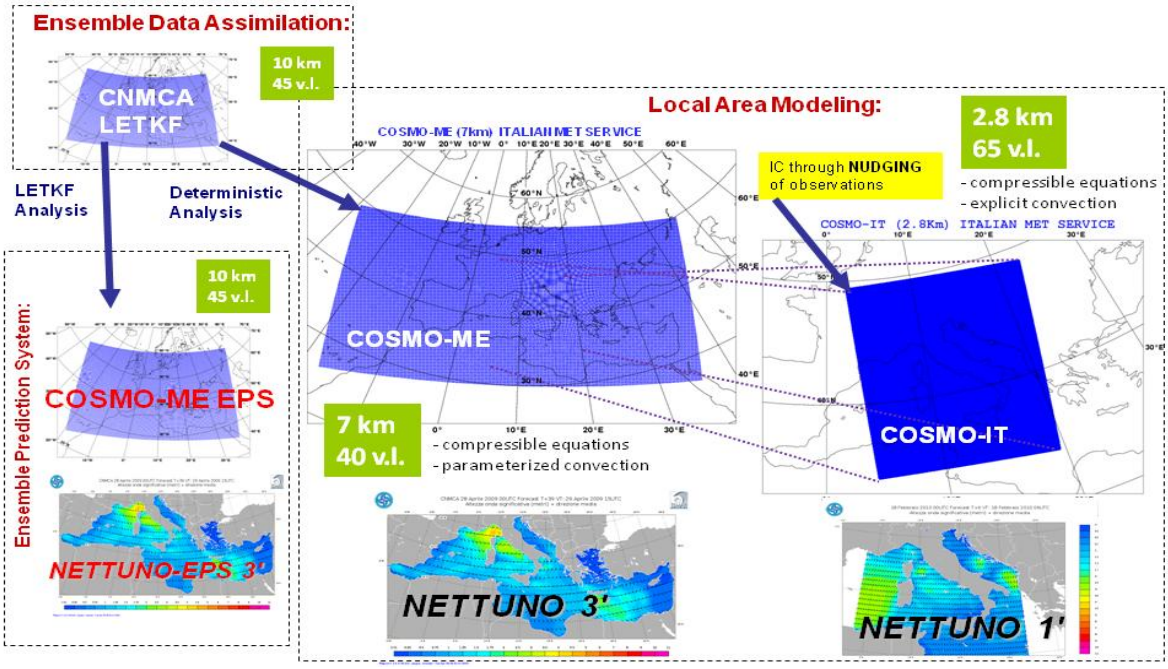

Fig.1: Schematic view of the operational Italian Air Force Met Service NWP system.

References

[1] Bonavita M, Torrisi L, Marcucci F. 2008. The ensemble Kalman filter in an operational regional NWP system: Preliminary results with real observations. *Q. J. R. Meteorol. Soc.* 134, 1733-1744.

[2] Bonavita M, Torrisi L, Marcucci F. 2010. Ensemble data assimilation with the CNMCA regional forecasting system. *Q. J. R. Meteorol. Soc.* 136, 132-145.

[3] Hunt, B. R., E. Kostelich, I. Szunyogh. "Efficient data assimilation for spatiotemporal chaos: a local ensemble transform Kalman filter", *Physica D*, 230, 112-126, 2007

[4] Whitaker, J. S., T. M. Hamill " Evaluating Methods to Account for System Errors in Ensemble Data Assimilation". *Mon. Wea. Rev.*, 140, 3078–3089, 2012

[5] Bertotti, L; Cavaleri, L; Loffredo, L.; Torrisi, L (2013). "Nettuno: analysis of a wind and wave forecast system for the Mediterranean Sea". Mon. Weather Rev. 141(9)

Assimilation of Himawari-8 atmospheric motion vectors into JMA's operational global, mesoscale and local NWP systems

Koji Yamashita

Numerical Prediction Division, Japan Meteorological Agency
e-mail: kobo.yamashita@met.kishou.go.jp

1. Introduction

The Meteorological Satellite Center of the Japan Meteorological Agency (JMA) has produced operational Himawari-8 atmospheric motion vectors (AMVs) since July 7th 2015 (Bessho et al. 2016). These are based on three sequential satellite images taken at intervals of 10 minutes, as opposed to the 30 – 60 minute intervals of images used for MTSAT-2 AMVs.

Himawari-8 AMVs will be assimilated into JMA's operational global, mesoscale and local numerical weather prediction (NWP) systems (see the JMA website[1]) in place of MTSAT-2 AMVs in March 2016. A specific quality control (QC) system has been created to enable the use of Himawari-8 AMVs in operational global and mesoscale four-dimensional variational data assimilation systems (GSM-DA and MSM-DA) and in the operational local three-dimensional variational data assimilation system (LFM-DA). Observing system experiments (OSEs) for Himawari-8 AMVs were performed over periods of one and two months using the GSM-DA, MSM-DA and LFM-DA systems with this QC approach in the winter and summer of 2015.

2. Characteristics of Himawari-8 AMV data

The characteristics of Himawari-8 AMVs were evaluated statistically against the first guesses of the GSM-DA, MSM-DA and LFM-DA systems. Figure 1 shows a histogram of the normalized difference (O-B) between the relevant wind speeds and first guesses in the GSM-DA system for the Northern Hemisphere (NH) at levels above 400 hPa from February 5 to March 20 2015. These were compared with O-B for MTSAT-2 AMVs, which are already assimilated in the operational GSM-DA and MSM-DA systems. As shown in Fig. 1, the histograms of O-B for NH AMVs in the GSM-DA system exhibit Gaussian distribution. Those for other regions and those in the MSM-DA and LFM-DA systems have the same characteristics (not shown). The standard deviation (STD) of O-B is around 0.5 m/s less than that of the MTSAT-2 AMVs, suggesting improved data quality. Data coverage is also improved (Fig. 2).

3. QC for Himawari-8 AMV data and OSEs

To support the effective use of Himawari-8 AMVs, the AMV pre-processing system has been updated in three main ways.

First, the quality indicator (QI, Holmlund 1998) thresholds for low-quality AMV rejection were revised in consideration of Himawari-8 AMV characteristics. Second, climatological checking was revised to involve the use of more AMVs in the middle troposphere. Third, a 100-km super-observation technique (Yamashita 2014) was introduced into the global NWP system for Japan and the surrounding areas. Details of other QC measures are provided on the NWP SAF AMV monitoring page[2].

To determine the impact of Himawari-8 AMVs with the revised pre-processing system in comparison with that used for MTSAT-2 AMVs, OSEs were performed for the periods from January to February 2015 (winter 2015) and from July to September 2015 (summer 2015).The term TEST is used to refer to the experiments with assimilation of Himawari-8 AMVs and without that of MTSAT-2 AMVs, and CNTL is used to refer to those with assimilation of MTSAT-2 AMVs. The results of two tests were compared, and other observations were used in both experiments as in the actual operational systems.

4. OSE results

The OSEs performed with the global NWP system revealed reduced O-B wind speed differences between TEST and CNTL over the Himawari-8 observation area (especially around Japan; Fig. 3). Figure 4 shows the normalized RMSE difference around Japan between TEST and CNTL forecasts covering periods from one to eleven days for 850 hPa wind vectors in summer 2015. Significant improvements (up to 3 – 6% on average) are seen until two-day forecasts for summer 2015. Positive or neutral impacts are seen for other physical elements and heights/regions. Mean positional errors for ten typhoons in summer were also reduced with 24-hour to 48-hour and 90-hour to 120-hour forecast

[1] http://www.jma.go.jp/jma/en/Activities/nwp.html
[2] http://research.metoffice.gov.uk/research/interproj/nwpsaf/satwind_report/amvusage/jmamodel.html

lead times. The reduction was around 6% with 24-hour to 48-hour forecast lead times (Fig. 5). The OSEs conducted with JMA's mesoscale and local NWP systems also showed improvement in rain forecasting (Fig. 6). Positive impacts on most physical elements and heights in the Southern Hemisphere were also seen in four-day forecasts for winter 2015 (not shown).

Himawari-8 AMVs with the revised pre-processing system are scheduled for assimilation into JMA's operational NWP systems in March 2016.

References

Bessho, K., K. Date, M. Hayashi, A. Ikeda, T. Imai, H. Inoue, Y. Kumagai, T. Miyakawa, H. Murata, T. Ohno, A. Okuyama, R. Oyama, Y. Sasaki, Y. Shimazu, K. Shimoji, Y. Sumida, M. Suzuki, H. Taniguchi, H. Tsuchiyama, D. Uesawa, H. Yokota and R. Yoshida, 2016: An introduction to Himawari-8/9 – Japan's new-generation geostationary meteorological satellites. J. Meteor. Soc. Japan, 94

Holmlund, K., 1998: The utilization of statistical properties of satellite-derived atmospheric motion vectors to derive quality indicators. Wea. Forecasting, 13, 1093 – 1104

Yamashita, K., 2014: Observing system experiments of MTSAT-1R rapid scan AMVs using JMA's operational NWP system from 2011 to 2013. Proc. 12th Int. Winds Workshop, Copenhagen, Denmark, EUMETSAT

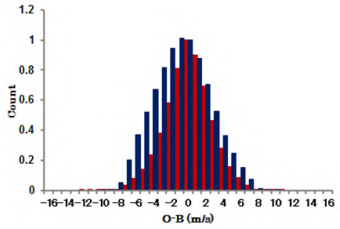

Figure 1. O-B normalized histograms of infrared AMVs at levels above 400 hPa in the Northern Hemisphere (poleward of 20°N) from February 5 to March 20 2015. The red and blue bars correspond to Himawari-8 and MTSAT-2 AMVs, respectively.

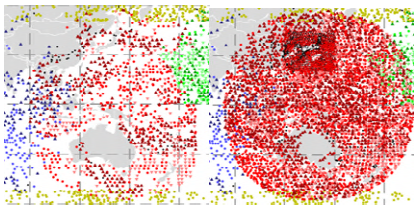

Figure 2. Assimilated AMV data coverage in the GSM-DA system for the 60°S – 60°N and 90°E – 170°W region at 00 UTC on July 20 2015. Left: MTSAT-2 AMVs (red plots); right: Himawari-8 AMVs (red plots).

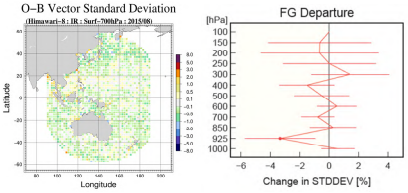

Figure 3. O-B wind speed differences between Himawari-8 and MTSAT-2 AMVs below 700 hPa for summer 2015 (left; negative values indicate better scores) and normalized O-B wind speed standard deviation differences between TEST and CNTL against wind profiler observations for summer 2015 (right; negative values indicate better scores, error bars represent a 95% confidence interval, and red dots indicate statistical significance).

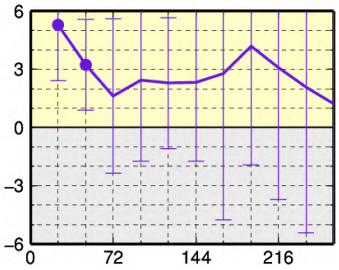

Figure 4. Normalized RMSE differences (y-axis) around Japan between TEST and CNTL covering periods from one to eleven days (x-axis) for 850 hPa wind vectors in summer 2015. Positive values indicate better scores. Error bars represent a 95% confidence interval, and dots indicate statistical significance.

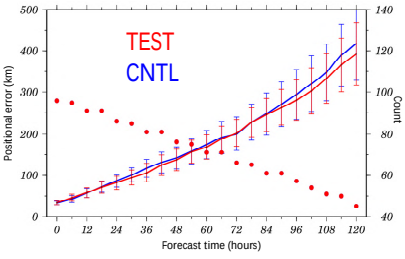

Figure 5. Average typhoon track forecast errors for summer 2015. The red line is for TEST values, the blue line is for CNTL values, and the red dots are sample data numbers. Error bars represent a 95% confidence interval.

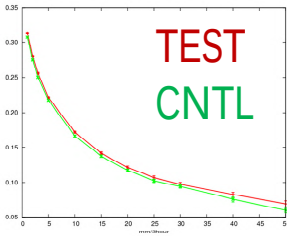

Figure 6. Equitable threat scores against radar-rainfall composite precipitation for each threshold of precipitation for summer 2015